Decoding the Temporal Diagnostics of Lyman Continuum Escape from High-Redshift Galaxies

A Thesis

submitted to
Indian Institute of Science Education and Research Pune in partial fulfilment of
the requirements for the BS–MS Dual Degree Programme
by

Parth Mehrotra

University of Texas at Dallas
800 W. Campbell Road
Richardson, TX
United States - 75080

Indian Institute of Science Education and
Research Pune
Dr. Homi Bhabha Road,
Pashan, Pune 411008, India

May 2026

Superviser:
Dr Aaron Smith
University of Texas at Dallas, United States

Certificate

This is to certify that the thesis entitled **Decoding the Temporal Diagnostics of Lyman Continuum Escape from High-Redshift Galaxies** towards the partial fulfilment of the BS-MS dual degree programme at the Indian Institute of Science Education and Research, Pune represents work carried out by **Parth Mehrotra** at the **University of Texas at Dallas, United States**, under the supervision of **Prof. Aaron Smith, Assistant Professor, Department of Physics** during the academic year **2025–2026**.

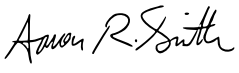

Prof. Aaron Smith

Prof. Surabhi Jaiswal

Prof. Prasad Subramaniam

Committee:
Prof. Aaron Smith
Prof. Surabhi Jaiswal
Prof. Prasad Subramaniam

“A dream is not something you see in sleep
A dream is something that does not let you sleep”
– Dr. APJ Abdul Kalam

.....
Dedicated to all my family and friends,
And to all those who doubt themselves,
Just keep pushing, and it’ll all fall in place
.....

Declaration

I hereby declare that the matter embodied in the report entitled **"Decoding the Temporal Diagnostics of Lyman Continuum Escape from High-Redshift Galaxies"** are the results of the work carried out by me at the Department of Physics, **University of Texas at Dallas, United States**, under the supervision of **Prof. Aaron Smith**, and the same has not been submitted elsewhere for any other degree. Wherever others contributed, every effort is made to indicate this clearly, with due reference to the literature and acknowledgement of collaborative research and discussions.

Parth Mehrotra
20211046

Acknowledgements

This thesis marks the culmination of a five-year journey and, hopefully, the beginning of a much longer one devoted to understanding the intricacies of the universe. The path has not always been smooth, and there were moments of turbulence along the way. However, persistence, perseverance, and the guidance of many remarkable people helped me navigate those challenges. While the journey was not easy, it has provided invaluable experience and has strengthened my resilience for the future.

I would like to express my sincere gratitude to my supervisor, **Prof. Aaron Smith**, for his constant guidance, support, and encouragement throughout my thesis work. His valuable suggestions and insights were instrumental in shaping this thesis. I am deeply thankful to him for giving me the opportunity to work under his mentorship. The lessons I learned during this time will remain with me throughout my career. I would also like to extend my gratitude to **Prof. Prasad Subramaniam**, who is an excellent mentor and guide, and his guidance helped me rectify my methods and allowed me to become a better research scholar.

I would also like to express my heartfelt gratitude to **Prof. Surabhi Jaiswal**, who accepted me as an intern and gave me the opportunity to begin my journey as a researcher and contribute to her work. Her encouragement, support, and words of wisdom provided guidance during some of the most challenging moments of my academic journey.

I would also like to extend my gratitude to **Dr. Evan Aguirre**, who made me believe in my skills, and would like to thank **Dr. Kuntal Mishra** for offering me an opportunity to work when I needed it the most.

I am grateful to the faculty and staff of the **Department of Physics, IISER Pune** and the **Department of Physics, University of Texas at Dallas** for providing an excellent academic and research environment. I would also like to thank the friends I made along the way, especially the LKG group, who made discussions, classes, and life at IISER more enjoyable and gave me countless memorable moments and lifelong anecdotes.

A special mention goes to Nerat Kapoor, Vikas Kapoor, and Manav Gogia for making my time in Pune memorable, filled with laughter, travel, and experiences I will always cherish. I would always crave those late night drives, and gaming sessions. I would also like to thank Srashti Agarwal, my best friend, who has seen me grow throughout this journey and has always stood by me during both the highs and the lows.

I would like to give a special mention to my aunt, Mrs. Viraj Mehrotra, and my uncle, Mr.

Mohit Mehrotra, who welcomed me with open arms and helped me cope with the challenges of a new country. Their children, Rajit Mehrotra, Ovi Mehrotra, and Ira Mehrotra, never made me feel 'out of place' and alone in a new country. They gave me great experiences and lifelong memories, which I will cherish all through my life.

Finally, I would like to express my deepest gratitude to my parents, Mrs. Ruchi Mehrotra and Dr. Pavan Kumar, and my sister, Pihu Mehrotra, as well as my extended family, for their unwavering support, encouragement, and patience throughout my journey. Without their love and belief in me, this work would not have been possible. I hope this thesis marks the beginning of a fulfilling career and that I will be able to live up to the opportunities that have been entrusted to me.

Finally, I would also like to acknowledge the assistance of modern tools, including ChatGPT, Gemini, and GoogleLM, which have helped me brainstorm ideas, improve the clarity of writing, and proofread sections of the thesis.

Contents

List of Figures

List of Tables

Abstract

The Epoch of Reionization (EoR) marks a critical phase in cosmic history, driven by the escape of Lyman Continuum (LyC) radiation from early galaxies. At redshifts $z > 6$, direct observations of LyC are suppressed by the neutral intergalactic medium, making it essential to understand the physical processes that regulate ionizing photon escape. In this work, we investigate these processes using high-resolution radiative transfer calculations applied to cosmological galaxy simulations, focusing on both statistical correlations and time-dependent behavior.

We show that the escaping ionizing photon rate $\dot{N}_{\rm LyC}^{\rm esc}$ strongly tracks the intrinsic production rate $\dot{N}_{\rm LyC}^{\rm int}$, reflecting the most recent underlying star formation activity, which provides the source of the LyC radiation. However, the escape fraction $f_{\rm esc}$ exhibits a delayed response, indicating that photon escape is regulated by the time required for stellar feedback to restructure the surrounding gas to create low-density channels. This demonstrates that LyC escape is governed by a combination of prompt source variability and delayed environmental response.

We further show that LyC escape is not steady but exhibits cyclic, feedback-driven variability. Phase-space analysis reveals quasi-periodic trajectories, while cross-correlation measurements confirm a systematic lag between star formation and escape. The characteristic timescales and regularity of these cycles depend on halo mass, with low-mass systems displaying highly stochastic behaviour and more massive systems more coherent cycles.

Overall, our results demonstrate that LyC escape is a coupled, time-dependent process shaped by both the source population and the evolving structure of the surrounding medium, providing a physically grounded framework for interpreting the contribution of galaxies to cosmic reionization.

Chapter 1

Introduction

1.1 Epoch of Reionization

The Epoch of Reionization (EoR) represents a major phase transition in the thermal and ionization history of the Universe, during which the predominantly neutral intergalactic medium (IGM) became ionized by the first luminous sources [2, 3]. Observations of high-redshift quasars indicate that reionization was largely complete by redshift $z \sim 6$, implying the existence of efficient sources of ionizing radiation at earlier cosmic times. Identifying these sources and understanding the mechanisms regulating their ionizing output remain central challenges in modern astrophysics [3, 2].

Star-forming galaxies at high redshift are widely believed to be the dominant contributors to the ionizing photon budget required for reionization [2, 3]. Massive stars in these galaxies produce copious Lyman continuum (LyC; $E > 13.6$ eV) photons capable of ionizing neutral hydrogen [4, 2]. However, only a fraction of these photons escape their host galaxies into the IGM. A significant portion is absorbed by neutral hydrogen and dust within the interstellar medium (ISM) and circumgalactic medium (CGM) [4]. The fraction of ionizing photons that successfully escape into the IGM, commonly referred to as the escape fraction ($f_{\rm esc,LyC}$), therefore plays a crucial role in determining the contribution of galaxies to cosmic reionization.

Despite its importance, the escape fraction remains poorly constrained both observationally and theoretically. Direct observations of LyC emission become increasingly difficult at $z \gtrsim 6$ because the neutral IGM is highly opaque to ionizing photons. Absorption by intervening neutral hydrogen produces the well-known Gunn–Peterson trough [5], which suppresses flux blueward of the Lyman-α transition. As a result, the ionizing radiation responsible for reionization cannot be directly observed at the redshifts where it occurred [3].

This observational limitation motivates the need for indirect tracers of LyC escape, as well as a deeper physical understanding of the processes that regulate it. While several galaxy properties have been proposed as potential diagnostics, the relationship between star formation activity and LyC escape remains complex and often exhibits significant scatter.

A key aspect that is often overlooked is the temporal dimension of this process. The escape of LyC photons is not instantaneous, but instead reflects the delayed response of the interstellar medium to episodes of star formation and feedback. Following a starburst, newly formed massive stars both produce ionizing radiation and drive feedback processes that progressively disrupt the surrounding dense gas. Only after this feedback has sufficiently cleared or redistributed the ISM do low-density channels form, allowing LyC photons to escape efficiently. This introduces a measurable time lag between star formation activity and LyC escape.

Capturing this time-dependent behaviour is therefore essential for developing a predictive framework for LyC escape. Understanding these processes requires detailed modelling of both the multiphase ISM and the radiative transfer of photons through complex galactic environments [4, 3].

1.2 Radiative Transfer

Radiative transfer (RT) provides the theoretical framework that connects the intrinsic properties of astrophysical systems to the radiation that ultimately reaches an observer [6, 1]. In the context of high-redshift galaxies, RT governs how ionizing photons propagate through the dense and inhomogeneous ISM before escaping into the IGM [7].

The evolution of the radiation field is described by the radiative transfer equation (RTE), which tracks the change in specific intensity $I_\nu \equiv I(r,t;\hat{n},\nu)$ at a given position r and time t per unit direction $\hat{n}$ and ν frequency as radiation propagates through a medium that emits, absorbs, and scatters photons:

$$\frac{1}{c}\frac{\partial I_\nu}{\partial t} + \mathbf{n}\cdot\nabla I_\nu = \eta_\nu - \chi_\nu I_\nu \,. \tag{1.1}$$

Here η_ν denotes the emissivity of the medium and χ_ν represents the extinction coefficient, which includes both absorption and scattering processes. A useful quantity in this context is the optical depth $\tau_\nu \equiv \int \chi_\nu \, \mathrm{d}\ell$, which measures the cumulative opacity along a photon's path and determines the probability of interaction with the medium.

Solving the radiative transfer equation in realistic astrophysical environments is computationally challenging due to its high dimensionality and the complex geometries involved. Modern simulations typically employ two broad classes of numerical methods: moment-based radiative hydrodynamics solvers and Monte Carlo radiative transfer techniques.

Moment-based methods evolve angular moments of the radiation field and are well suited for coupling radiation with hydrodynamical evolution in large cosmological simulations. In contrast, Monte Carlo radiative transfer (MCRT) techniques track discrete photon packets as they propagate through the simulation domain. MCRT methods are particularly well suited for modeling detailed spectral features and complex scattering processes, making them ideal for producing synthetic observations.

In this work, MCRT calculations play a central role in linking the underlying physical

properties of simulated galaxies to observable quantities, enabling a direct investigation of how ionizing radiation escapes through a dynamically evolving and multiphase ISM.

1.3 Monte Carlo Radiative Transfer

Monte Carlo radiative transfer (MCRT) solves the radiative transfer problem using a stochastic approach. Instead of directly solving the integro-differential transfer equation, the radiation field is represented by a large number of discrete photon packets whose trajectories and interactions are determined probabilistically [1].

Each packet is initialized with properties such as position, direction, frequency, and weight sampled from the emissivity distribution of the radiation sources. As the packet propagates through the medium, the optical depth to the next interaction is drawn from an exponential probability distribution

$$\tau = -\ln \xi \,,$$

where ξ is a uniformly distributed random number in the interval $[0, 1)$. The corresponding physical distance traveled depends on the local opacity of the medium.

When an interaction occurs, the packet may either be absorbed or scattered depending on the local albedo of the material. In scattering events the packet's direction and frequency can change according to the relevant physical processes. By repeating this procedure for a sufficiently large number of packets, the global radiation field and emergent spectra can be reconstructed.

Modeling radiation transport in galaxies also requires accounting for gas motions. Many modern radiative transfer codes therefore employ a mixed-frame approach in which photon packets are propagated in the laboratory frame while interactions are computed in the local comoving frame of the gas. This treatment self-consistently captures Doppler shifts and other velocity-dependent effects that shape spectral line profiles.

By combining these techniques, MCRT provides observational signatures, bridging the gap between the complex hydrodynamics of simulations like THESAN-ZOOM and the observable spectral features detected by telescopes like the *JWST* [8, 9].

1.4 This Work

In recent years, numerical simulations have demonstrated that the escape of ionizing radiation from galaxies is highly anisotropic and strongly time-dependent. Stellar feedback processes such as radiation pressure, stellar winds, and supernova explosions can disrupt dense star-forming regions and temporarily create low-density channels through which ionizing photons escape. As a result, the LyC escape fraction can fluctuate significantly on timescales of tens of megayears. Understanding the temporal connection between star formation activity and

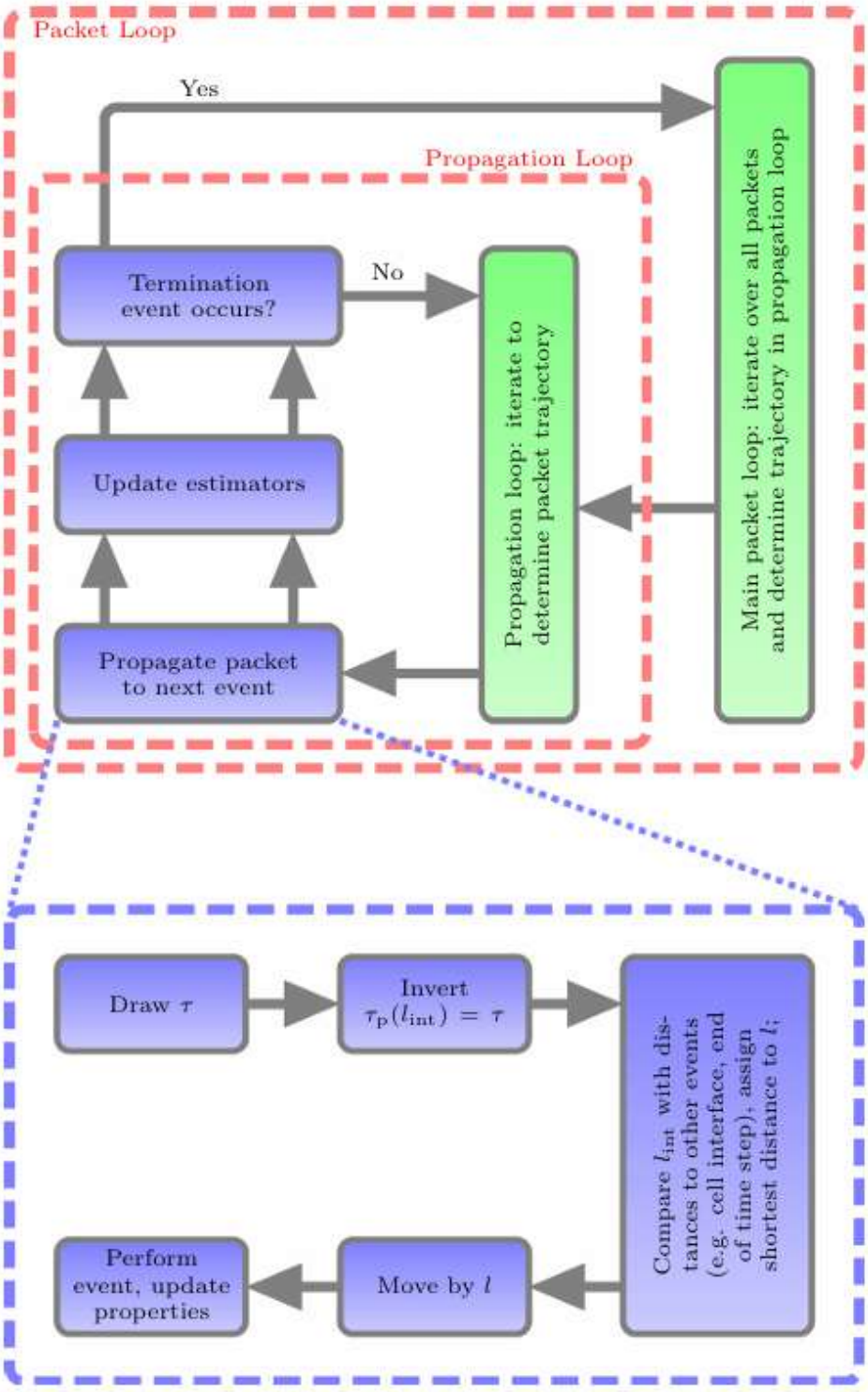

Figure 1.1: Schematic overview of the Monte Carlo radiative transfer (MCRT) algorithm. ** This figure has been directly adopted from [1].

LyC escape is therefore essential for interpreting both theoretical models and observational diagnostics.

This thesis focuses on the intersection between simulations and observations by investigating observable secondary tracers of LyC escape. While direct measurements of LyC radiation are not possible at the redshifts relevant to the Epoch of Reionization, several observable galaxy properties can provide indirect information about the processes regulating ionizing photon escape. In particular, quantities such as the star-formation rate (SFR $\equiv \Delta M_\star/\Delta t$) averaged over different timescales (SFR_{10} and SFR_{100} for 10 and 100 Myr), the specific star-formation rate (sSFR $\equiv \mathrm{SFR}/M_\star$), the offset from the star-forming main sequence (Δ_{MS} relative to the overall population) provide immediate insights into the physics but are not direct observables. While quantities such as the ultraviolet (L_{UV}), Balmer-alpha ($L_{\mathrm{H}\alpha}$), and Lyman-alpha ($L_{\mathrm{Ly}\alpha}$) luminosities can be measured observationally, they can be connected to the SFR on different timescales and therefore provide a bridge to the physical parameters that can easily be obtained from simulations to observables.

These quantities probe different timescales of star formation and feedback. The short-timescale star formation rate, SFR_{10}, is closely linked to nebular emission lines such as Hα, whose luminosity ($L_{\mathrm{H}\alpha}$) traces the presence of massive, short-lived stars and therefore the instantaneous ionizing photon production rate. In contrast, the ultraviolet continuum luminosity (L_{UV}) traces star formation over longer timescales of $\sim$ 50–100 Myr and is therefore more closely associated with SFR_{100} [10]. Similarly, Lyα luminosity ($L_{\mathrm{Ly}\alpha}$) provides additional information about the ionizing radiation field and the distribution of neutral gas surrounding star-forming regions. Because these observables are routinely measured in high-redshift galaxy surveys, they provide a natural framework for interpreting simulation results in an observational context.

To investigate these connections, we analyze galaxies from the THESAN-ZOOM simulation suite, which provides high-resolution ($\sim$ 17 pc) radiation-hydrodynamical models of galaxies at $z > 3$. These simulations incorporate detailed treatments of stellar feedback, multi-phase ISM structure through the SMUGGLE model, and self-consistent dust evolution. The simulation outputs are post-processed using the Monte Carlo radiative transfer code COLT, which generates synthetic spectra and allows us to directly measure the LyC escape fraction, described in more detail in Chapter 2.

Using these mock observations, we first investigate correlations between LyC escape and physical parameters that might act as a secondary tracer. We then explore the temporal relationship between LyC escape and star formation activity by analyzing the time evolution of the escape fraction alongside star formation indicators such as the burstiness parameter sSFR defined as the ratio of $\mathrm{SFR}_{10}/\mathrm{SFR}_{100}$.

To quantify the time-dependent behaviour of these quantities, we employ a combination of phase-space analysis, peak-trough analysis, and cross-correlation techniques. In particular, we use Fourier-based methods to measure characteristic periodicities and determine the time

lag between physical parameters related to star formation and LyC radiation. This framework allows us to identify feedback-driven cycles and quantify the delay between star formation episodes, ISM restructuring, and the resulting escape of ionizing radiation (see Chapter 3).

Chapter 2

Methods

2.1 Simulations

2.1.1 THESAN-ZOOM

The THESAN-ZOOM project consists of a suite of high-resolution, radiation-hydrodynamical zoom-in simulations designed to investigate the formation and evolution of galaxies at $z > 3$. These galaxies are selected from the parent THESAN simulation volume, a large-scale (95.5 cMpc) radiation-magnetohydrodynamic project that models the Epoch of Reionization (EoR). THESAN/* simulations are built with the AREPO moving mesh code and follows ΛCDM cosmology. It assumes the required cosmological parameters from the Planck Collaboration: $H_0 = 100h$, where $h = 0.6774$, $\Omega_m = 0.3089$, $\Omega_\Lambda = 0.6911$, $\Omega_b = 0.0486$, $\sigma_8 = 0.8159$ and $n_s = 0.9667$.

By utilising the zoom-in technique, THESAN-ZOOM enhances the resolution of 14 regions within the original THESAN simulations, allowing us to probe galaxy-scale phenomena and properties during the EoR. It offers three different resolutions within the simulation, which enhance spatial resolution by factors of 4, 8, and 16, resulting in increases in mass resolution by factors of 64, 512, and 4096, respectively. It results in a baryonic mass resolution of $9.09 \times 10^3\,\mathrm{M}_\odot$, $1.14 \times 10^3\,\mathrm{M}_\odot$, and $142\,\mathrm{M}_\odot$, respectively, for the three resolution levels, allowing for a detailed treatment of the multi-phase ISM, while preserving the cosmological properties and large-scale structures from the parent simulations [11, 8].

The simulations solves the radiation-hydrodynamic equations on an unstructured Voronoi mesh. A defining characteristic of THESAN-ZOOM is its unique treatment of the large-scale radiation field. Rather than adopting a spatially uniform UV background, the simulations leverage the radiation field topology of the parent THESAN volume as time-varying boundary conditions. This approach self-consistently models patchy reionization, enabling galaxies to be reionized by external sources in an "outside-in" manner.

The baryonic physics is governed by a significantly modified version of the SMUGGLE model. This includes a non-equilibrium thermochemical network that explicitly tracks molecu-

lar hydrogen (H_2), self-consistent dust evolution (production, accretion, and destruction) [12], and various stellar feedback channels such as supernovae, radiation pressure, stellar winds, and photoionisation. By injecting momentum into the surrounding gas on short timescales, these processes prevent the catastrophic overcooling of the interstellar medium and regulate the conversion of cold gas into stars. This ensures that the simulated galaxies maintain a realistic gas-to-stellar mass ratio, providing a physically consistent counterpart to the high-redshift systems observed by the *James Webb Space Telescope*.

Name	**Group ID**	**Alias**	**4x**	**8x**	**16x**
m13.0	39	B	✓	×	×
m12.2	205	C	✓	×	×
m11.9	578	D	✓	×	×
m11.5	1163	E	✓	×	×
m11.1	5760	F	✓	✓	×
m10.8	10304	G	✓	✓	×
m10.4	33206	H	✓	✓	×
m10.0	37591	I	✓	✓	×
m9.7	137030	J	✓	✓	✓
m9.3	500531	K	✓	✓	✓
m8.9	519761	L	✓	✓	✓
m8.5	2274036	M	✓	✓	✓
m8.2	5229300	N	✓	✓	✓

Table 2.1: Summary of simulation runs and resolution scales.

Halos are identified using the friends-of-friends (FOF) algorithm, with self-gravitating halos within these groups are identified using the SUBFIND-HBT algorithm. In this work, we focus on all 13 available halos in the simulation suite and run at all available resolutions, spanning a redshift range of 3 to 16. Various halos, their corresponding aliases used in the simulations, and the available resolutions for each halo are shown in Table 2.1. The Sim name encodes the halo mass at the lowest redshift, with the number specifying the exponential power. For instance, Halo B (m13.0) means that the mass of that halo will reach $10^{13}\,M_\odot$ at redshift 3.

2.1.2 COLT

To bridge the gap between simulation and observation, we employ the COLT (Cosmic Lyman-α Transfer) code, a massively parallel Monte Carlo radiative transfer (MCRT) framework. COLT is designed to stochastically solve the radiative transfer equation by propagating individual photon packets through complex, multi-phase media. The packets are initialised with positions, directions, and frequencies, and are then propagated through an adaptive three-dimensional Voronoi grid. This approach is particularly advantageous for high-redshift galaxy formation studies, as it naturally handles non-spherical geometries, resonant scattering, and frequency-dependent opacities that are otherwise challenging for deterministic solvers.

A fundamental feature of COLT is its implementation of the mixed-frame approach for moving media. Photons are tracked in the laboratory frame to maintain spatial accuracy on the simulation grid, while radiation–matter interactions are treated in the local comoving frame (CMF) of the gas cells. This allows for the precise characterization of spectral line profiles shaped by H II regions, supernova remnants, and galactic-scale outflows, including Doppler shifts and line broadening. To ensure the physical accuracy of these signatures, we utilize COLT to perform post-processing photoionization equilibrium calculations. This iterative procedure self-consistently determines the ionization states of hydrogen, helium, and various metal species (e.g., Si II, C II) based on the local radiation field sourced from stellar populations [13, 5].

COLT leverages the next-event estimation (peel-off) technique. This variance reduction method calculates the probability of each photon scattering toward a specific observer at every interaction point, enabling the construction of high-resolution, low-noise mock spectra and surface brightness maps along arbitrary lines of sight. By incorporating self-consistent dust evolution and continuous absorption modeling, COLT provides a rigorous framework for investigating the correlations between observable stellar continuum absorption and the underlying escape fraction of ionizing radiation. Postprocessing THESAN-ZOOM simulations with COLT, allow us to generate an entire catalogue of galaxy observations spanning the redshift range, $3 < z < 16$. To run COLT we need to first specify the configurations corresponding to the line, physical processes, instrument aperture and frequency ranges, and other restrictions we wish to include in the parameter files to simulate different halo observations. The various configurations that we ran are described in the next section, and this work will focus on the outputs of the `Lya` (Lyα), `Ha` (Hα), `M1500` ($M_{\rm UV}$ at 1500 Å), `ion-eq` (photoionization equilibrium), and `proj` (projected column density) runs, with a few relevant parameters taken from configurations like `Hb` (Hβ), `OII-3727-3730` (O II doublet), `OIII-5008` (O III) spectral lines. Along with these, we also ran and catalogued configurations such as `optical` ($M_{\rm opt}$ at 5000 Å), `SiII-1190` (Si II), `Ha-cont` (Hα stellar continuum), and `Lya-cont` (Lyα stellar continuum) for the aforementioned halos for work to be carried out in the future. As part of the thesis, I was thoroughly trained and made significant contributions to the necessary COLT pipelines and source code to obtain the synthetic observations.

2.2 COLT Runs

To generate mock observations from the THESAN-ZOOM suite, we employed the COLT radiative transfer code. Each simulation requires specific configurations to define initial photon packets, dust properties, and required analytical outputs. Prior to these runs, the parameters for the Graphite, PAH, and Silicate dust models were updated; these revised tables provide updated values for opacities (κ), albedos, and scattering asymmetry parameters ($\langle\cos\theta\rangle$). Furthermore, the implementation was generalized to support the simultaneous inclusion of multiple dust species.

2.2.1 Lyman-alpha Transfer

This configuration executes a full Monte Carlo radiative transfer (MCRT) simulation of Lyman-alpha emission, modeling the production and transport of Lyα photons in a self-consistent physical framework. The simulation incorporates recombination emission (with a 7000 K line ratio temperature floor) and collisional excitation, propagating photons through gas capped at 10^6 K to maintain numerical stability. Dust attenuation is treated explicitly using metallicity-based grain tables (graphite, silicate, and PAH).

To optimize computational efficiency, resonant scattering is accelerated via dynamical core-skipping, while a 10 km/s microturbulent velocity is applied to broaden the Doppler profile. The run utilizes 10^6 photon packets with a luminosity boosting factor of $j_{\rm exp} = 0.75$. Photons are emitted within half the bounding box and are considered "escaped" upon crossing a spherical boundary at $0.75 \times R_{\rm box}$. Outputs include angle-averaged spectra resolved over $\pm$3000 km/s (600 bins), high-resolution projected images, and Healpix-based escape fraction maps, making this setup ideal for studying the morphology of extended Lyα halos.

2.2.2 Balmer-alpha Transfer

The Balmer-alpha (Hα) configuration models the production and propagation of Balmer-alpha photons. Unlike the resonant Lyα line, Hα transport is primarily governed by dust absorption and scattering rather than frequency diffusion. Emission is sourced from hydrogen recombinations and collisional excitations, capturing contributions from both star-forming H II regions and shock-heated gas.

To achieve high statistical convergence, we utilize a significantly larger photon count of 5×10^7 packets ($j_{\rm exp} = 0.75$). The simulation resolve the line over $\pm$500 km/s across 500 bins. Spatially, it generates 512^2 resolution projected images and IFU-like spectral cubes. This setup is optimized for comparing intrinsic recombination signatures against dust-attenuated observables, providing a high signal-to-noise view of the Hα structure in high-redshift galaxies.

2.2.3 M1500 Continuum

This module computes the dust-processed stellar UV radiation near 1500 Å to determine the rest-frame UV magnitude (M_{1500}). Rather than a line-transfer approach, this utilizes COLT's ionization equilibrium module in a single-pass mode (`max_iter = 1`). Stellar emission is drawn from BPASS libraries (Chabrier IMF) with age-metallicity dependence, restricted to a narrow wavelength window (1475–1525 Å).

Notably, all gas ion species are disabled to treat the medium as a purely attenuating dust screen without photoionization feedback. By utilizing 5×10^7 packets, the simulation produces robust statistics for intrinsic and escaped UV luminosities. These results allow for the calculation of UV escape fractions and the characterization of anisotropic attenuation profiles relative

to the galaxy's stellar core.

2.2.4 Ionization Equilibrium (ion-eq)

The `ion-eq` configuration models the hydrogen and helium ionization structure by tracking stellar ionizing radiation. Photons are propagated using 5×10^7 packets with adaptive frequency binning (`ion_bins = true`, max width 0.05 dex) to resolve ionization edges. While H I, He I, and He II photoionization are tracked, metal ions remain disabled.

With `max_iter = 1`, this run serves as a single-pass evaluation of the radiation field rather than a fully converged equilibrium solution. The escape boundary is set to a tighter radius ($0.25 \times R_{\rm box}$) to specifically probe ionizing leakage from the interstellar medium into the inner halo. The resulting diagnostics quantify the competition between gas and dust absorption in regulating the escape of Lyman-continuum radiation.

2.2.5 Geometric Projections (proj)

The `proj` configuration utilizes a ray-based module for purely geometric analysis, independent of Monte Carlo scattering. It generates 4K resolution (3840×2160 pixels) maps of gas density (ρ) and squared density (ρ^2), where the latter emphasizes high-density clumping and star-forming regions.

The module employs a perspective camera setup with a 0.5 stepback factor, integrating through a spherical volume. To ensure temporal consistency for potential visualization or movie generation, the camera rotates azimuthally across snapshots (`rotate_with_snaps: true`). This configuration provides a clear structural baseline of the galaxy's morphology, facilitating a direct comparison between the underlying gas distribution and the emergent light profiles.

2.2.6 Supplementary Runs

Apart from these configurations we also ran the following configurations, but they are not the focus of this thesis, although a few results might have been utilised while running the analysis-

1. **Hα-continuum**
   This COLT configuration simulates the continuum surrounding the Balmer-alpha line within a cosmological galaxy snapshot by incorporating stellar continuum emission. In contrast to pure line-emission runs, recombination and collisional Hα production are disabled. Instead, the continuum flag activates broadband stellar radiation within $\pm$1500 km/s of the line center, utilizing BPASS stellar population synthesis (Chabrier IMF) in the stellar rest frame. Photons originate from these realistic stellar spectra and propagate through the gaseous medium, where the emergent spectrum is shaped by Hα resonant scattering (with dynamical core-skipping) and dust interaction. All other parameters remain identical to the pure line-emission model.

2. **Lyα-continuum**
   This configuration models the continuum surrounding the Lyman-alpha line. Similar to the Hα variant, recombination and collisional Lyα production are deactivated in favor of broadband stellar radiation within $\pm$2500 km/s of the line center. Sourced from BPASS tables, these photons undergo full Lyα resonant scattering and dust attenuation. By employing dynamical core-skipping, the simulation efficiently captures how the gas and dust distribution modify the underlying stellar continuum. Consistent with previous runs, all remaining physical conditions are held constant relative to the pure line-emission case.

3. **OII-3727-3730**
   The Monte Carlo radiative transfer calculations are performed using COLT in order to model the emission and propagation of the [OII] doublet from simulated galaxies. Spectral quantities are sampled across a velocity range of -600 to 400 km/s with hundreds of frequency bins, enabling detailed reconstruction of the emergent line profiles, while keeping rest of the physical conditions consistent with rest of the runs.

4. **OIII-5008**
   The Monte Carlo radiative transfer calculations are performed using COLT in order to model the emission and propagation of the [OIII] 5008 A line from simulated galaxies. Spectral quantities are sampled across a velocity range of -500 to 500 km/s with hundreds of frequency bins, enabling detailed reconstruction of the emergent line profiles, while keeping rest of the physical conditions consistent with rest of the runs.

5. **Hβ**
   The MCRT module models the emission and propagation of Balmer-β photons within the simulated galaxy. Consistent with previous runs, all remaining physical conditions are held constant relative to the pure line-emission Hα case.

After running these configurations, we move to the Results, where we first look at the various projections and images of a halo under various configurations, and plot the fluxes of the respective lines in order to verify that the run successfully runs on all the halos and configurations.

Chapter 3

Results and Discussion

Following the successful execution of the simulations and the completion of the radiative transfer post-processing using COLT, this chapter presents a detailed analysis of the resulting data. We begin by examining the fundamental outputs of the radiative transfer calculations in order to establish a physical baseline for the simulated galaxies before focusing specifically on the properties of the escaping Lyman Continuum (LyC) radiation.

The initial stage of the analysis investigates the statistical relationships between various galactic parameters in order to identify potential correlations. A primary objective of this study is to determine which observable quantities may act as reliable secondary tracers to various properties related to LyC radiation. This is particularly important for interpreting high-redshift observations, where direct detection of LyC photons is often strongly suppressed by absorption in the intergalactic medium.

Subsequently, we examine the cyclic behaviour of the LyC escape fraction ($f_{\mathrm{esc,LyC}}$) in relation to the burstines parameter (sSFR). This motivates a deeper investigation of the temporal dynamics governing LyC escape. Furthermore, we perform a time-lag and peak-to-peak analysis by comparing fluctuations in $f_{\mathrm{esc,LyC}}$ with variations in the star formation rate averaged over different timescales (SFR_t). By analysing the relative timing between these quantities, we aim to quantify the delayed response between star formation activity and the escape of ionizing radiation, thereby probing the role of stellar feedback in regulating the escape of LyC photons from galaxies.

3.1 Projections

Using the projections module of COLT, we generate two-dimensional gas density squared ρ^2 projections from the simulation outputs, as illustrated in Figure 3.1. The flexibility of COLT allows the construction of projections not only for the gas density distribution, which provides a visual representation of the halo morphology, but also for other physical parameters such as the neutral hydrogen fraction ($x_{\mathrm{H\,I}}$) and gas temperature.

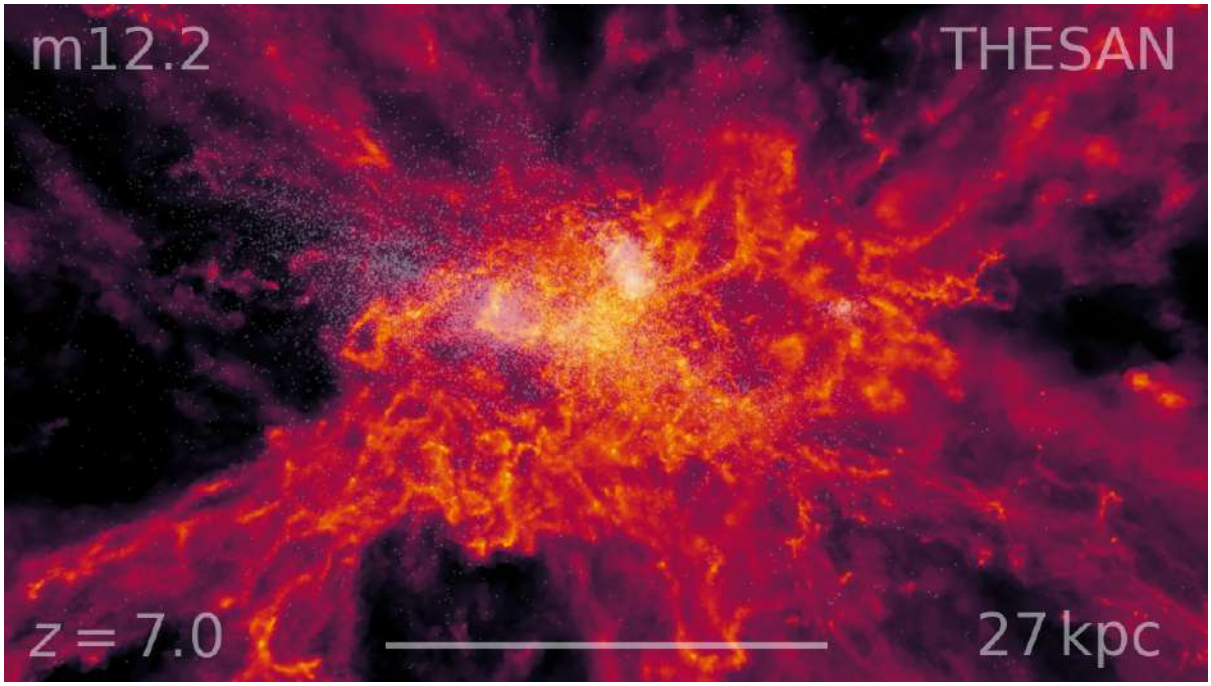

Figure 3.1: Projection of the gas distribution (ρ^2) for a simulated galaxy (C4) at redshift $z = 7$.

This pipeline incorporates a recentering algorithm, a recalculation of the virial radius, and a temporal interpolation scheme between simulation snapshots. Such visualizations are useful both for identifying dynamical events such as mergers and for providing intuitive insight into the morphological evolution of the simulated galaxies. An example frame generated using this procedure is shown in Figure 3.1.

3.2 Simulated observational signatures

3.2.1 Fluxes

To verify the physical consistency of the radiative transfer calculations, we examine the simulated emission-line fluxes produced by COLT. In particular, we analyze the Lyman-α (Lyα) and Balmer-α (Hα) transitions, whose spectral profiles are expected to differ significantly due to the distinct radiative transfer processes governing each line.

The Lyα line undergoes resonant scattering with neutral hydrogen atoms. As Lyα photons propagate through the interstellar and circumgalactic media, repeated scattering events cause the photons to diffuse both spatially and in frequency before escaping the galaxy. Consequently, the emergent Lyα spectrum typically exhibits a broadened and asymmetric profile, often characterized by a double-peaked structure with a suppressed line center. The separation and relative strength of these peaks depend sensitively on the neutral hydrogen column density, gas kinematics, and dust content. For example, outflowing gas can preferentially enhance the red peak while suppressing the blue peak, as Doppler shifts allow redshifted photons to escape

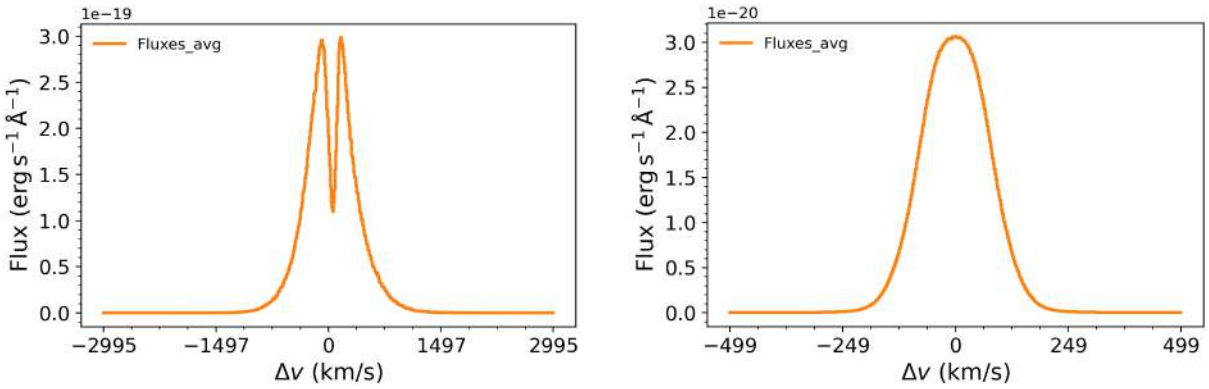

(a) Simulated Lyα flux profile showing the broadened and asymmetric structure.

(b) Simulated Hα flux profile displaying a comparatively symmetric shape

Figure 3.2: Comparison of simulated emission-line flux profiles generated with COLT. The Lyα profile reflects the complex radiative transfer effects associated with resonant scattering, whereas the Hα profile retains a simpler structure characteristic of recombination emission.

more efficiently.

In contrast, Hα photons originate from recombination within ionized H II regions and do not experience resonant scattering. As a result, the Hα line profile generally remains comparatively simple and symmetric, typically approximating a Gaussian distribution centered near the systemic velocity of the galaxy. Its width is primarily determined by thermal broadening, turbulent motions, and large-scale gas dynamics.

The simulated flux profiles produced by COLT, as seen in Figure 3.2, reproduce these theoretical expectations, providing an important validation that the radiative transfer calculations capture the essential physical processes governing the propagation of these emission lines.

3.2.2 Healpix Maps

To study the angular distribution of escaping radiation, we construct maps using the `HEALPix` (Hierarchical Equal Area isoLatitude Pixelization) framework. `HEALPix` provides an equal-area tessellation of the sphere, allowing the full sky surrounding the galaxy to be divided into discrete angular pixels with uniform solid angle. Each escaping photon packet is assigned to a `HEALPix` pixel according to its direction of propagation at the escape boundary, enabling the construction of directional maps of flux, escape fraction, and spectral properties.

This approach is particularly well suited for studying anisotropic radiation escape, as it preserves angular information while allowing statistical averaging within each pixel. The angular resolution of the maps is controlled by the parameter $N_{\rm side}$, which determines the total number of pixels on the sphere according to $N_{\rm pix} = 12N_{\rm side}^2$. The value of $N_{\rm side}$ is specified within the COLT configuration files.

The expected morphology of `HEALPix` maps differs substantially between Lyα, Hα, and LyC radiation due to their distinct interactions with the surrounding medium. Lyα photons,

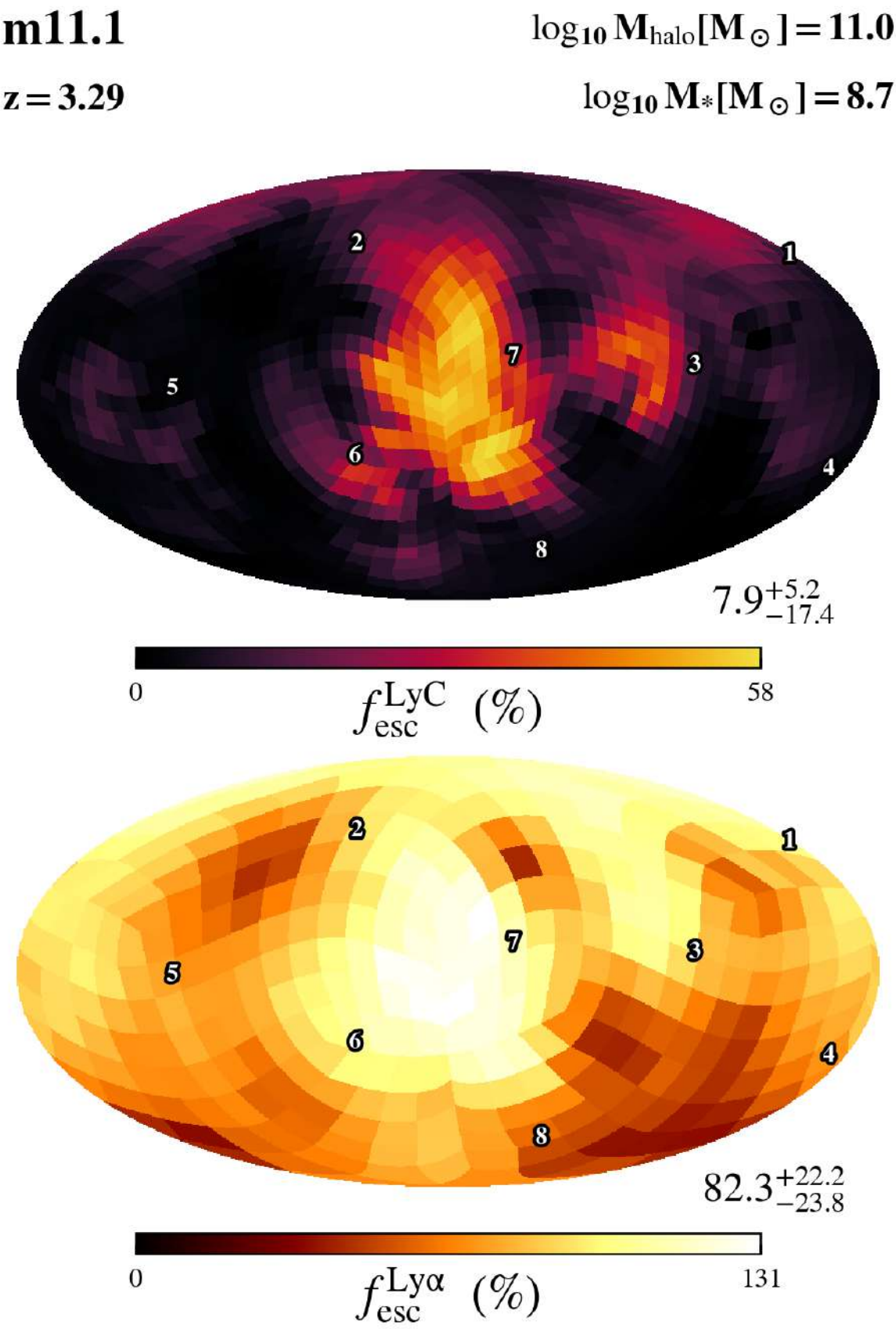

Figure 3.3: HEALPix projections showing the angular distribution of escaping radiation.

which undergo repeated resonant scattering, tend to produce relatively smooth and extended angular distributions as multiple scattering events isotropize the radiation field. Nevertheless, residual anisotropies may persist due to large-scale gas flows, density inhomogeneities, or preferential escape channels.

Hα photons, by contrast, propagate largely without scattering and therefore trace the intrinsic distribution of ionized star-forming regions more directly. In the absence of significant dust attenuation, the resulting Hα `HEALPix` maps exhibit a bright and relatively isotropic distribution. In the simulations, the dust distribution and efficient destruction during feedback events leads to low dust absorption. As a result, the Balmer emission remains effectively optically thin and dust-related attenuation plays a negligible role in the analysis presented here.

LyC photons behave very differently. Because they are readily absorbed by neutral hydrogen, LyC radiation can escape only through low-column-density pathways within the interstellar and circumgalactic media. Consequently, LyC `HEALPix` maps are typically highly anisotropic, often dominated by a small number of bright pixels corresponding to ionized escape channels or "escape cones."

Figure 3.3 illustrates this contrast by comparing the angular distribution of escaping radiation in the simulated galaxy. The morphology of the maps highlights the distinct radiative transfer physics governing each emission component.

3.2.3 Images

To connect the intrinsic physical state of the simulated galaxy with observable emission properties, we generate multi-directional image projections using `COLT`. Eight virtual cameras are placed around the galaxy, each viewing the system from a different direction, which are also depicted on the `HEALPix` maps depicted in Figure 3.4. This setup allows us to examine how the observed morphology varies with viewing angle.

Figure 3.4 presents a set of multi-panel image strips showing several key emission tracers, including Lyα, Hα, rest-frame optical light, the mid-ultraviolet (MUV), and the diagnostic line ratios O_{32} and R_3. Examining these tracers simultaneously provides insight into the distribution of stellar populations, the kinematics of the gas, and the ionization state of the interstellar medium (ISM).

- **Rest-frame Optical and MUV**

  The rest-frame optical continuum traces the established stellar mass distribution and reveals the large-scale morphology of the galaxy. In contrast, the MUV emission is dominated by the youngest and most massive stellar populations. Differences between the optical and MUV morphologies highlight localized regions of active star formation that drive stellar feedback processes within the galaxy.

- **Hα vs. Lyα Emission**

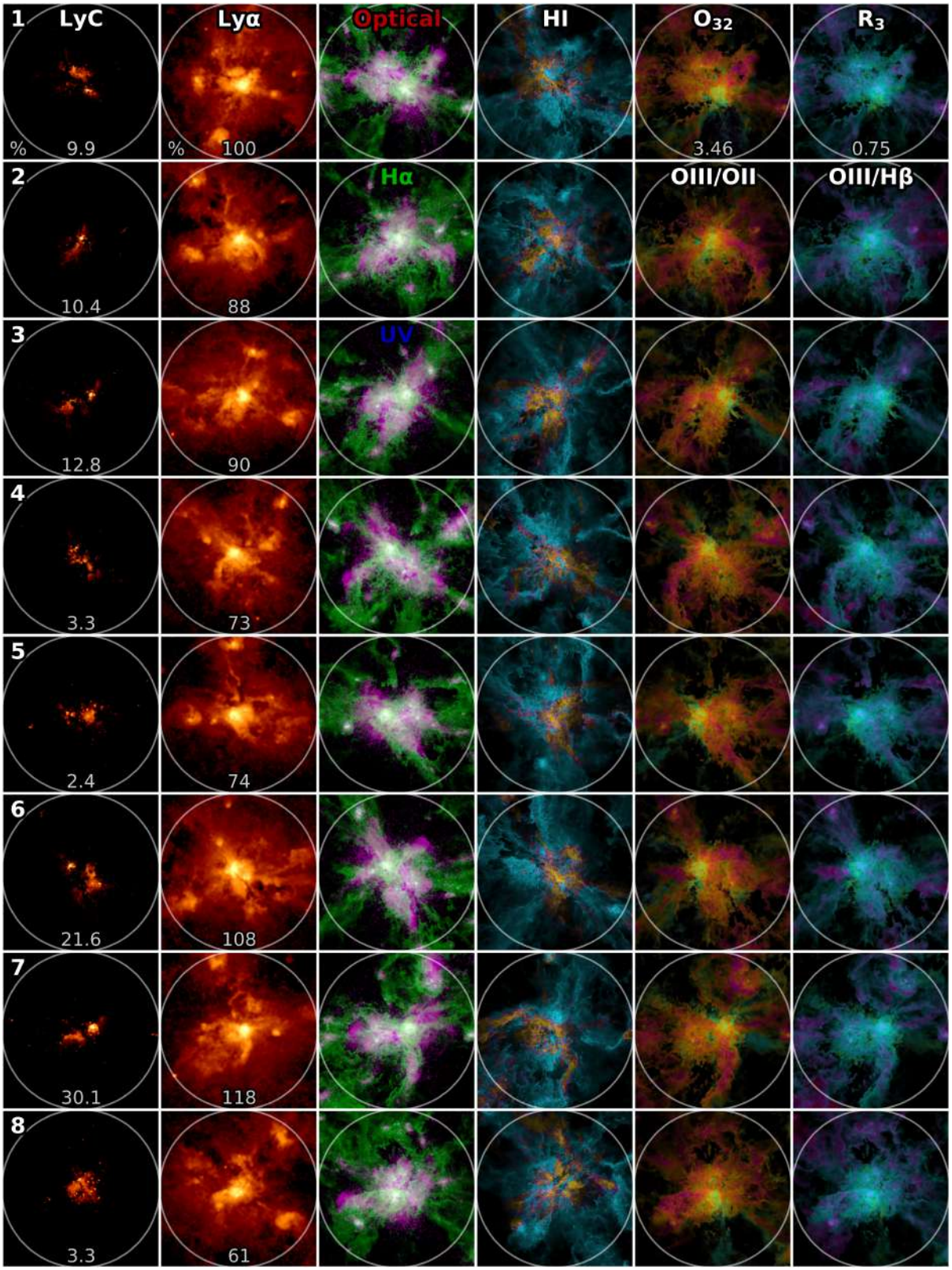

Figure 3.4: Image strip showing the observable halo from the 8 cameras setup through COLT

Both Hα and Lyα emission trace recent star formation, yet their spatial distributions differ significantly due to radiative transfer effects. The Hα emission outlines the immediate surroundings of ionized H II regions and closely traces the instantaneous star formation rate. Lyα emission, however, appears substantially more extended because Lyα photons scatter resonantly off neutral hydrogen in the circumgalactic medium. As a result, Lyα maps often reveal large diffuse halos surrounding the compact star-forming regions.

- **Ionization Diagnostics: O_{32} and R_3**

  The emission-line ratios O_{32} ([O III]/[O II]) and R_3 ([O III]/Hβ) provide powerful diagnostics of the ionization state and excitation conditions of the gas. High R_3 values generally indicate highly excited, low-metallicity gas typical of intense starburst environments. The O_{32} ratio is particularly sensitive to the optical depth of the interstellar medium. Regions exhibiting extreme O_{32} values are indicative of highly ionized, density-bounded channels through which ionizing photons can escape. These structures often correspond to regions where stellar feedback has cleared neutral gas, thereby creating the physical pathways that allow Lyman Continuum radiation to escape from the galaxy.

Taken together, these image strips illustrate the spatial correlation between intense star formation (traced by bright MUV and Hα emission) and the feedback-driven clearing of the interstellar medium (highlighted by elevated O_{32} ratios). The extended Lyα halos visible in the images originate from the same compact star-forming regions responsible for the high-excitation nebular emission, demonstrating the complex interplay between stellar feedback, gas kinematics, and photon escape in high-redshift galaxies.

3.3 Secondary Tracers to Lyman Continuum

To investigate potential secondary tracers of Lyman Continuum (LyC) radiation, we perform a statistical analysis of correlations between LyC-related quantities and observable galaxy properties across the simulation dataset. Instead of treating each simulation output as an isolated scatter point, we construct two–dimensional frequency distributions (heatmaps) for pairs of parameters. This approach mitigates visual saturation in dense regions of parameter space and reveals the underlying structure of the data.

For each parameter pair, the data are discretized into bins to construct a two–dimensional histogram, with the color scale representing the number density of data points within each bin. A logarithmic normalization is applied to the color scale in order to capture the large dynamic range present in the simulated galaxy population. The correlations are evaluated against two key LyC-related quantities: the LyC escape fraction ($f_{\mathrm{esc,LyC}}$) and intrinsic and escaping LyC photon production rate ($\dot{N}_{\mathrm{LyC}}^{\mathrm{int/esc}}$).

To extract systematic trends from the stochastic scatter inherent in individual galaxies, we compute the median value of the dependent variable within bins of the independent parameter.

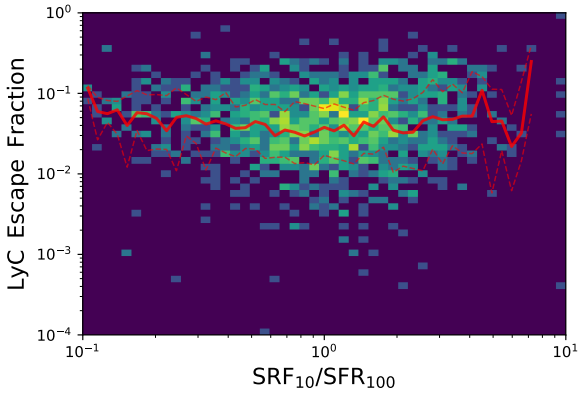

(a) Relationship between $f_{\mathrm{esc,LyC}}$ and the burstiness parameter.

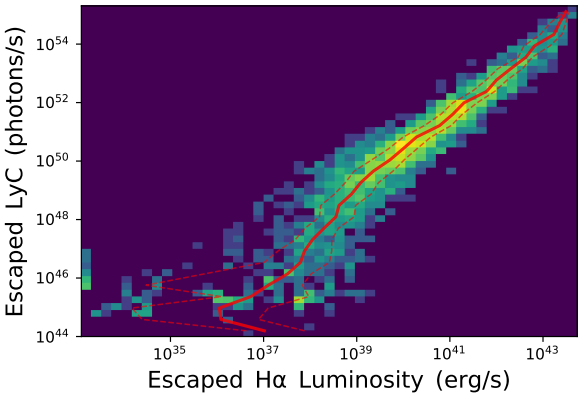

(b) Correlation between Hα luminosity and the escaping LyC photon production rate, $\dot{N}_{\mathrm{LyC}}^{\mathrm{esc}}$.

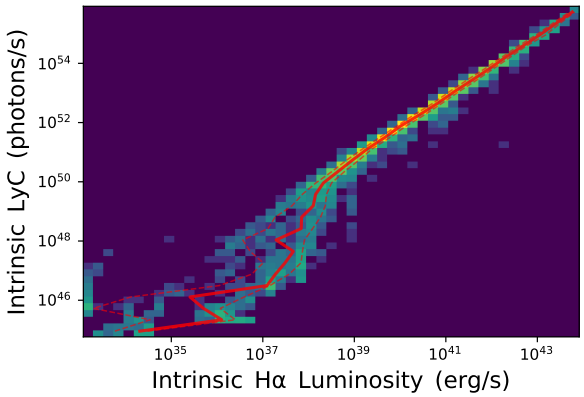

(c) Correlation between Hα luminosity and the intrinsic LyC photon production rate, $\dot{N}_{\mathrm{LyC}}^{\mathrm{int}}$.

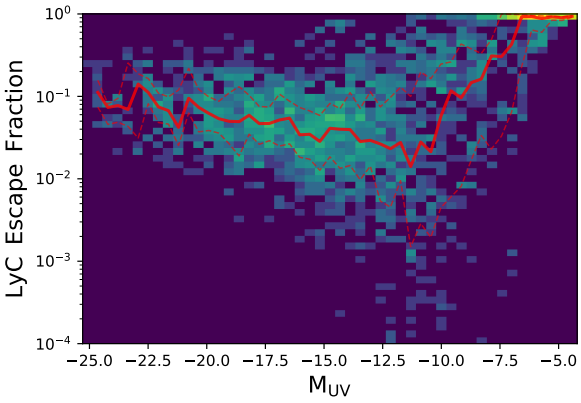

(d) Relationship between UV magnitude, M_{1500}, and the LyC escape fraction.

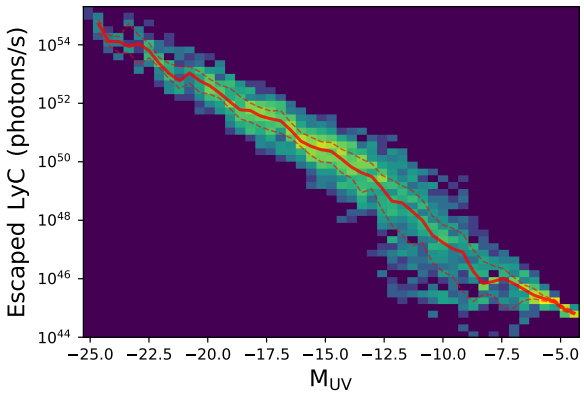

(e) Correlation between UV magnitude, M_{1500}, and the escaping LyC photon production rate.

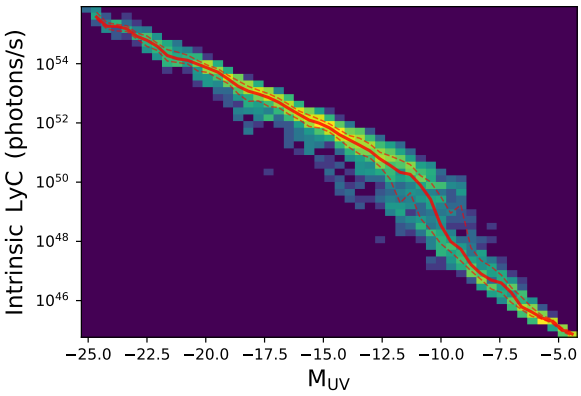

(f) Correlation between UV magnitude, M_{1500}, and the intrinsic LyC photon production rate.

Figure 3.5: Phase-space density distributions showing correlations between LyC-related quantities and observable tracers (Part I). The colour scale indicates the number density of points in each bin. The solid red curve shows the binned median trend, while the dashed curves mark the 25th and 75th percentiles.

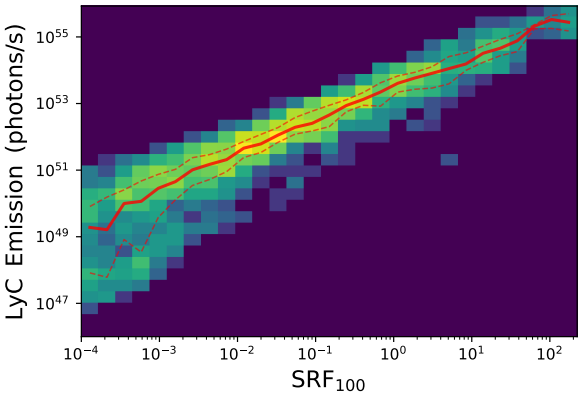

(a) Intrinsic LyC photon production rate versus SFR_{100}.

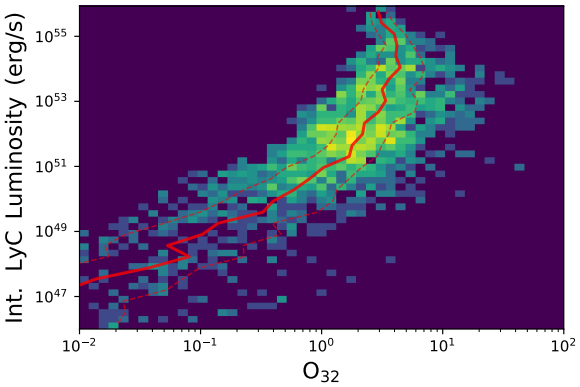

(b) Relationship between O_{32} and the intrinsic LyC photon production rate.

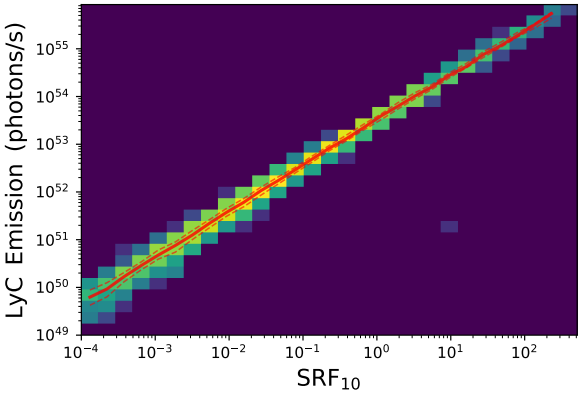

(c) Intrinsic LyC photon production rate versus SFR_{10}.

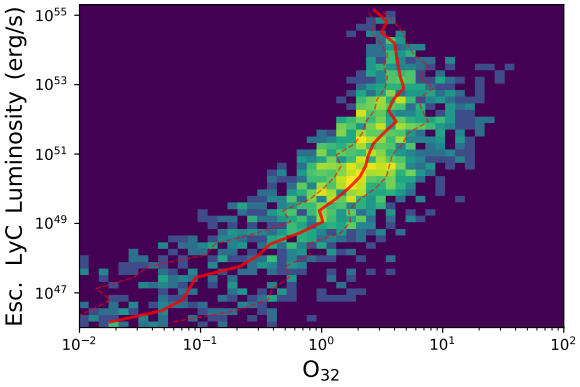

(d) Relationship between O_{32} and escaping LyC photon production rate.

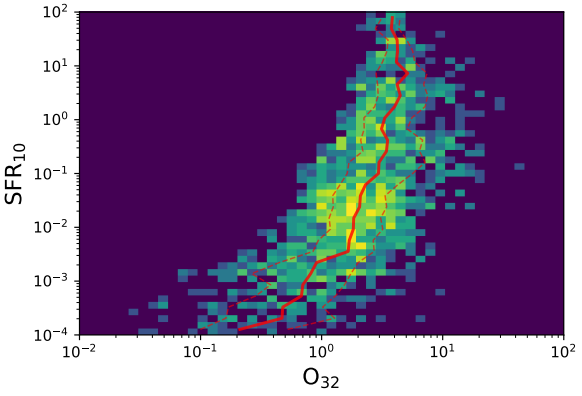

(e) Relationship between O_{32} and SFR_{10}.

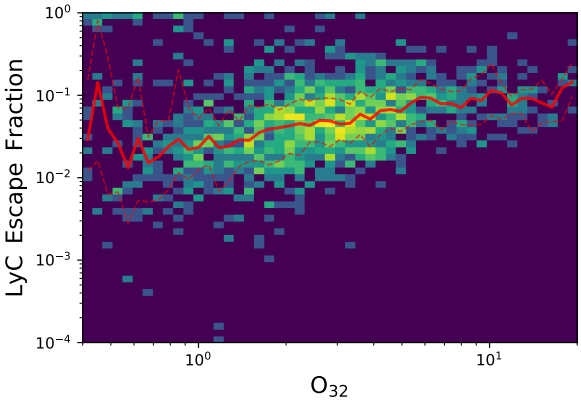

(f) Relationship between O_{32} and the LyC escape fraction.

Figure 3.6: Phase-space density distributions showing correlations between LyC-related quantities and secondary tracers (Part II).

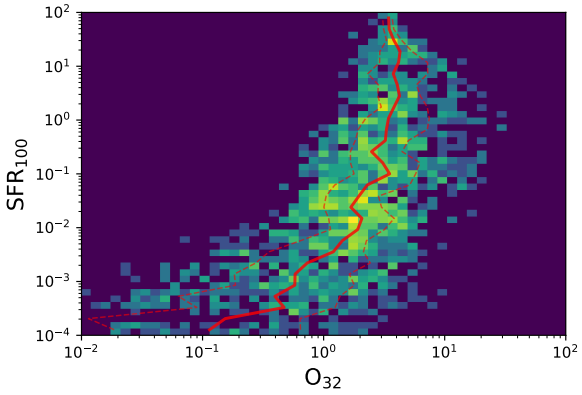

(a) Relationship between O_{32} and the star formation rate averaged over 100 Myr, SFR_{100}.

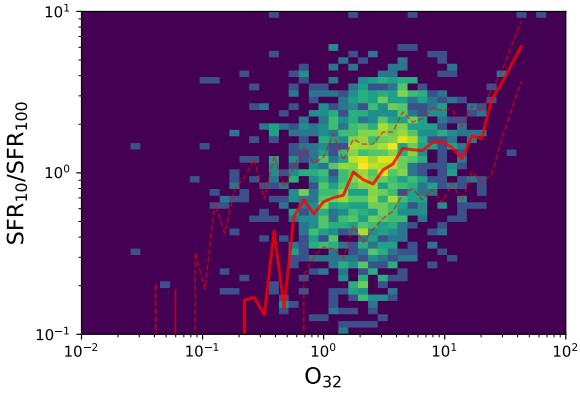

(b) Relationship between O_{32} and the star formation burstiness parameter

Figure 3.7: Phase-space density distributions showing the dependence of the ionization diagnostic.

The resulting median trendline represents the most probable relationship between the tracer and the LyC quantity. To quantify the dispersion around this relation, we additionally compute the 25$^{\text{th}}$ and 75$^{\text{th}}$ percentiles within each bin, defining the interquartile range (IQR). A narrow IQR indicates a strong and predictable correlation, whereas a wider IQR reflects significant physical scatter arising from variations in gas geometry, feedback strength, and interstellar medium structure.

To ensure statistical robustness, an occupancy threshold is imposed such that median and percentile statistics are calculated only for bins containing at least five data points. This prevents poorly sampled regions of parameter space from biasing the inferred trends.

The intrinsic LyC photon production rate $\dot{N}_{\text{LyC}}^{\text{int}}$ is stored directly within the COLT outputs for each simulation snapshot. The LyC escape fraction is defined as the ratio between the escaping and intrinsic photon fluxes, which allows the escaping photon emission rate to be calculated as

$$\dot{N}_{\text{LyC}}^{\text{esc}} = f_{\text{esc,LyC}} \times \dot{N}_{\text{LyC}}^{\text{int}} \,. \tag{3.1}$$

We explore correlations between these quantities and several physical tracers, including the star formation rate averaged over a timescale t (SFR_t) and the nebular emission-line ratio O_{32}. The time-averaged star formation rate is defined as

$$\text{SFR}_t = \frac{M_{\text{star}}(\text{age} < t)}{t} \,, \tag{3.2}$$

where $M_{\text{star}}[\text{age} < t]$ represents the total stellar mass within one virial radius with stellar ages less than t Myr.

The ionization-sensitive line ratio O_{32} is defined as

$$O_{32} = \frac{L_{[\text{O III}]\,5008}}{L_{[\text{O II}]\,3727,3730}} \,, \tag{3.3}$$

and is widely used as a diagnostic of the ionization parameter and optical depth of the interstellar medium. High values of O_{32} are often associated with density-bounded H II regions and have therefore been proposed as potential observational tracers of LyC escape.

In addition to the absolute star formation rate, the ratio between short- and long-timescale star formation indicators provides insight into the burstiness of star formation. In particular, the ratio between SFR_{10} and SFR_{100} traces rapid variations in star formation activity. Observationally, these timescales can be approximated using different spectral tracers: Hα emission traces very recent star formation (~ 10 Myr), while ultraviolet continuum emission traces stellar populations on longer timescales (~ 100 Myr) [10]. The ratio of these quantities is commonly referred to as the burstiness parameter (sSFR) and serves as a useful indicator of recent starburst activity.

Figures 3.5, 3.6 and 3.7 illustrate the resulting correlations between LyC quantities and several candidate secondary tracers. While many parameters exhibit some degree of correlation with $f_{\mathrm{esc,LyC}}$, $\dot{N}_{\mathrm{LyC}}^{\mathrm{int}}$, or $\dot{N}_{\mathrm{LyC}}^{\mathrm{esc}}$, the strength and reliability of these relationships vary significantly. In particular, certain tracers produce narrow interquartile ranges, indicating a tighter and more predictive relationship with LyC escape, whereas others show substantial scatter. These deviations from simple linear correlations reflect the complex interplay of gas dynamics, neutral hydrogen column density, and feedback-driven channel formation that ultimately regulate the escape of ionizing photons.

Motivated by these trends, we next focus specifically on the relationship between the burstiness ratio or parameter and the LyC escape fraction in order to investigate the temporal coupling between starburst activity and the escape of ionizing radiation.

3.4 Polar Analysis

We now shift our focus to studying the quasi-cyclic behaviour between the burstiness parameter (sSFR) and the LyC escape fraction. Since stellar populations are the primary sources of ionizing radiation, bursts of star formation naturally increase the number of young, massive stars capable of producing LyC photons. During such starburst episodes, the short-timescale star formation rate (SFR_{10}) increases significantly, resulting in an elevated sSFR leading to an increase in ionizing photon production, while the escape fraction responds with a delay as feedback processes gradually reshape the ISM and create low-density pathways.

Following the burst phase, stellar feedback processes, such as supernova explosions and stellar winds, begin to disperse the surrounding gas. This feedback suppresses further star formation by expelling the gas reservoir, leading to a quenching phase during which star formation declines. In this stage, the burstiness parameter decreases (sSFR < 1), but the ISM may remain porous for some time, allowing the escape fraction to remain elevated. Over time, gravitational forces cause the expelled gas to re-accrete toward the galaxy, eventually restoring the conditions required for another burst of star formation. This sequence of starburst, feedback-

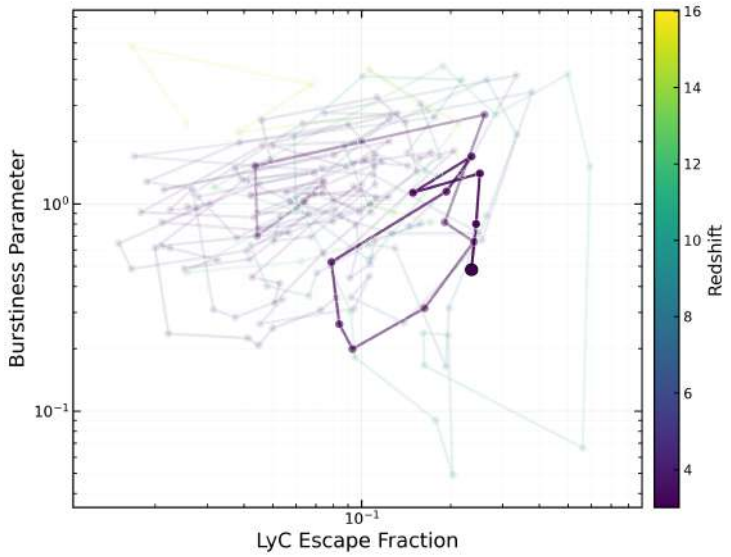

(a) Evolutionary track of a halo in the sSFR–$f_{\mathrm{esc,LyC}}$ phase space, illustrating the temporal evolution in the phase space

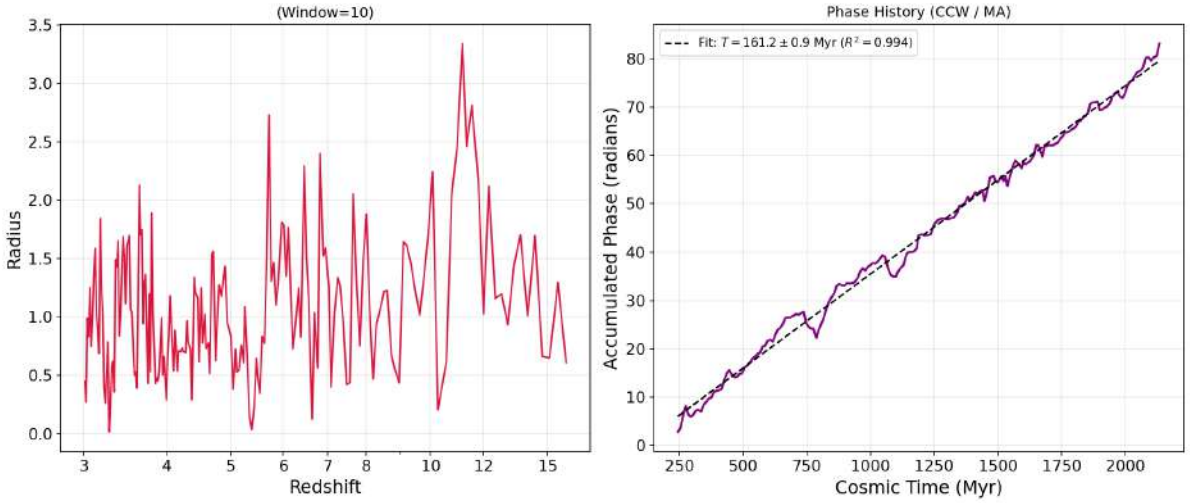

(b) Polar representation of the cyclic evolution between sSFR and $f_{\mathrm{esc,LyC}}$ for halo B4. The top panel shows the effective radius of the cycle, while the bottom panel shows the phase angle θ as a function of cosmic time.

Figure 3.8: Visualization of the quasi-cyclic relationship between burstiness parameter and LyC escape fraction.

driven clearing, and gas re-accretion drives recurrent, feedback-regulated cycles in the galaxy's evolutionary history, resulting in variability in the escape fraction.

To verify this quasi-cyclic behaviour, we first examine the evolution of $f_{\mathrm{esc,LyC}}$ and sSFR in phase space. We construct a scatter plot in which each point represents the pair ($f_{\mathrm{esc,LyC}}$, sSFR) for a given simulation snapshot. The colour of each point encodes its corresponding redshift, while a fading transparency track illustrates the system's temporal progression. As shown in Figure 3.8a, the evolutionary trajectory of a halo traces a loop-like pattern in phase space as the system evolves over cosmic time. Although the trajectory is not perfectly circular owing to variations in the strength of feedback processes and duration of starburst events, as well as changes in the gas distribution, it nevertheless reveals a loop-like structure indicative of cyclic behaviour.

To study this cycle more quantitatively, we transform the phase-space trajectory into polar coordinates. We construct a moving window of ten simulation snapshots and compute a moving average of the rescaled sSFR and $f_{\mathrm{esc,LyC}}$ values within this window. Prior to the transformation, both axes are normalized to lie between 0 and 1, ensuring that the resulting polar coordinates are dimensionless and comparable across different halos. The moving average within each window serves as an effective centre for the cycle. For each point in the window, we then compute the polar radius r and phase angle θ relative to this centre.

The radius r provides a measure of the extent of the trajectory in phase space, which can be interpreted as a proxy for the cycle amplitude, while the phase angle θ indicates the stage of the cycle corresponding to a given snapshot. The results for the massive halo B4 are shown in Figure 3.8b. The radial coordinate exhibits moderate fluctuations around a characteristic value of order unity. Some of the small-scale variations arise from the finite width of the moving window used to define the cycle centre, as well as variations in feedback strength and gas geometry.

In contrast, the phase angle θ shows an overall increasing trend with small fluctuations over cosmic time, reflecting the quasi-periodic progression of the system through successive starburst cycles. By fitting a linear relation to $\theta(t)$, we can estimate the characteristic period of this cycle. For halo B4, the derived period is approximately $161\,\mathrm{Myr}$, indicating that the coupled cycle of star formation activity and LyC escape repeats on this characteristic timescale.

Physically, this behaviour is expected for massive halos. Their large gas reservoirs enable relatively frequent starburst events, while their deep gravitational potential wells allow gas expelled by stellar feedback to re-accrete efficiently. This rapid recycling of gas shortens the interval between successive starburst episodes, thereby reducing the cycle period.

Extending this analysis to the full halo sample reveals a systematic dependence of the cycle period on galaxy mass. Lower-mass halos generally exhibit longer cycle periods, consistent with the expectation that their shallower gravitational potentials allow feedback-driven outflows to escape more easily and delay the re-accretion of gas required to trigger subsequent bursts, leading to more extended gas redistribution and delayed re-accretion, with the gas dynamics

exhibiting diffusion-like behaviour due to feedback-driven outflows.

When the derived cycle periods are plotted against stellar mass ($M_\star$) and halo mass ($M_{\rm halo}$), both relations exhibit approximately linear trends in logarithmic space, suggesting an approximate power-law scaling. The resulting scaling relations can be expressed as

$$T^{\rm sSFR}_{f_{\rm esc,LyC}} \propto M_\star^{-0.16} \qquad \text{and} \qquad T^{\rm sSFR}_{f_{\rm esc,LyC}} \propto M_{\rm halo}^{-0.22}\,. \tag{3.4}$$

These relations imply that more massive systems experience more frequent cycles in the parameter space, while lower-mass galaxies evolve on longer timescales. This behaviour is consistent with the theoretical picture in which the efficiency of gas recycling and the gravitational confinement of the interstellar medium increase with halo mass. Consequently, massive galaxies can replenish their star-forming gas reservoirs more rapidly, leading to shorter recurrence times for starburst events and the associated bursts of LyC escape. Although low-mass halos exhibit high cycle periods, they show some scatter and large errors. There are outliers as well, which show unphysical time periods, however using inverse variance weight-scaling, we ensure that the outliers do not bias the best-fit line plotted over the scatter points, suggesting that an underlying scaling relation may be present despite the observed scatter. This loop-like behaviour indicates that the escape fraction is not determined by the instantaneous star formation activity, but instead by the time-dependent evolution of the interstellar medium driven by stellar feedback.

3.5 Time Lag Analysis

The evolution of star-forming galaxies exhibits quasi-cyclic behaviour driven by the interplay among gas accretion, star formation, and stellar feedback. Periods of enhanced gas inflow trigger bursts of star formation, during which newly formed massive stars remain embedded within dense star-forming regions of the ISM. At this stage, the neutral hydrogen column density around the young stellar population is high, leading to low escape fractions of ionising radiation.

As stellar feedback in the form of radiation pressure, stellar winds, and supernova explosions progressively disrupts the surrounding gas, the ISM becomes more porous and low-density channels are created. These channels allow ionising photons to escape more efficiently, causing the LyC escape fraction to peak after star formation peaks. Eventually, as feedback weakens and gas re-accretes or redistributes within the galaxy, the ISM becomes denser again, reducing the escape of ionising radiation and initiating the next cycle of star formation. While we cannot directly observe the evolution of individual galaxies, the underlying feedback processes are fundamental and therefore the resulting behaviour predicted based on cosmological simulations is expected to be broadly applicable to star-forming galaxies.

This feedback-regulated process introduces a natural temporal offset between star formation

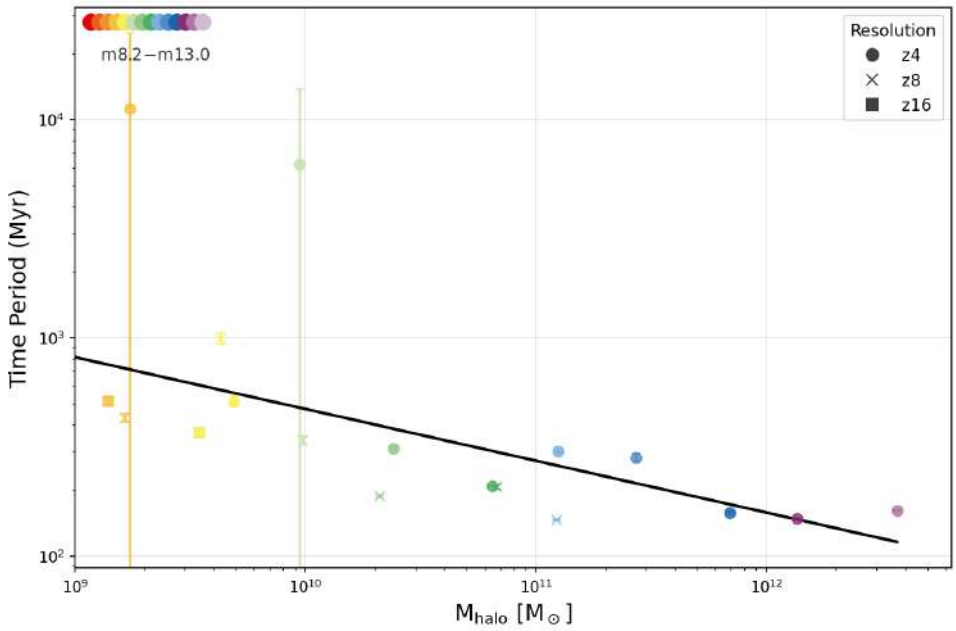

(a) Dependence of the starburst–LyC cycle period on halo mass M_{halo} for all simulated halos.

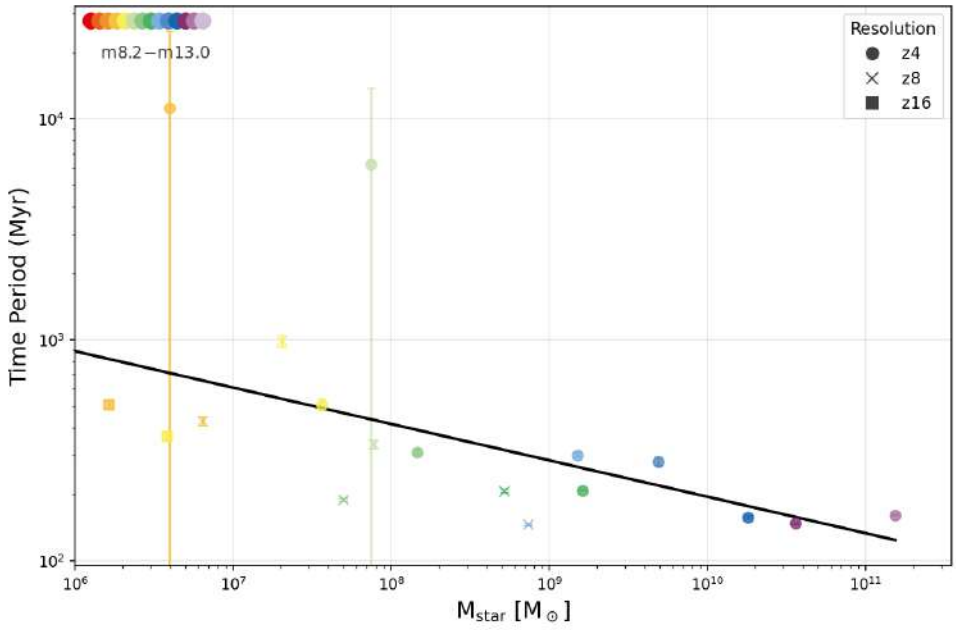

(b) Dependence of the cycle period on stellar mass $M_\star$.

Figure 3.9: Scaling relations between the characteristic cycle period of the sSFR–$f_{\mathrm{esc,LyC}}$ evolution and galaxy mass.

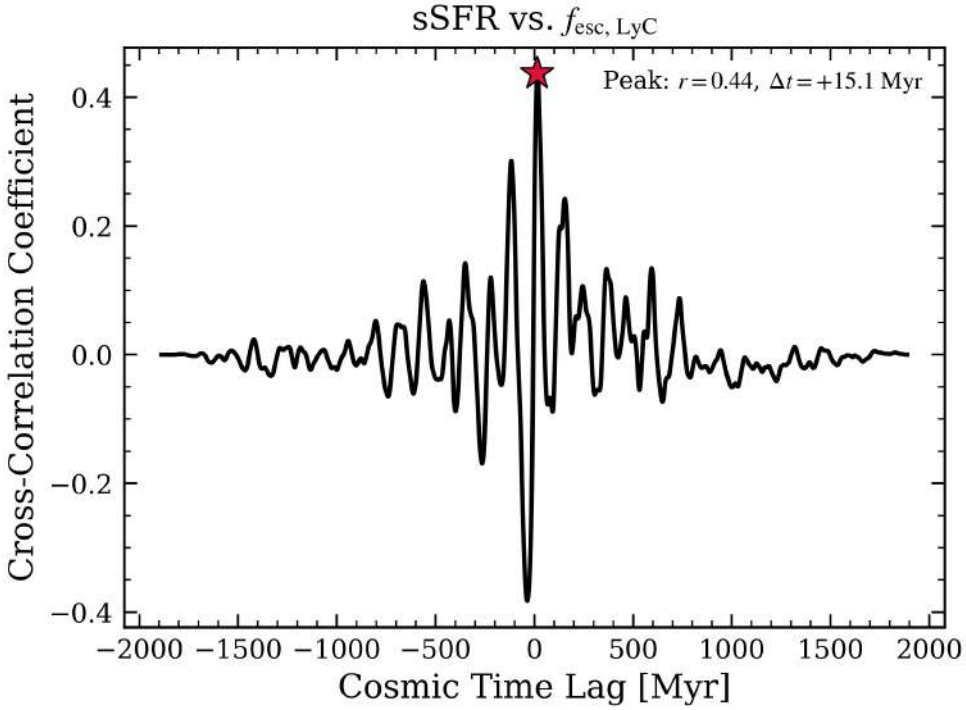

(a) Time-lag determination using the SUNKIT-IMAGE cross-correlation method for the relationship between sSFR and $f_{\mathrm{esc,LyC}}$.

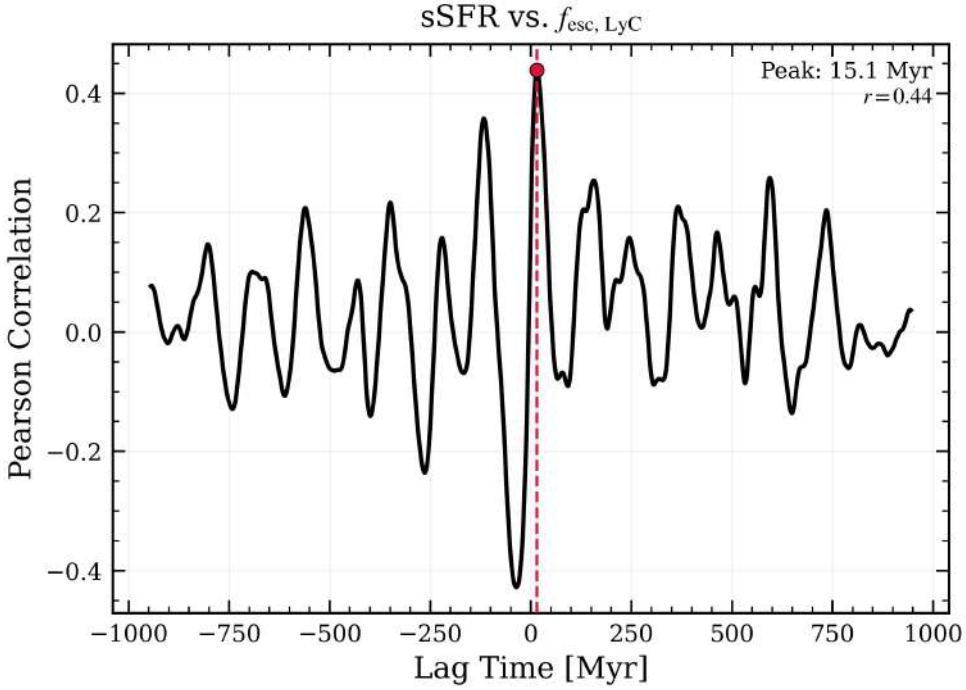

(b) Lag scan using the Pearson cross-correlation coefficient between sSFR and $f_{\mathrm{esc,LyC}}$.

Figure 3.10: Example time-lag analysis for halo B4 showing the cross-correlation between the burstiness parameter and the LyC escape fraction.

and the escape of ionising photons. To quantify this delay, we perform a time-lag analysis on the time series of the burstiness parameter and $f_{\mathrm{esc,LyC}}$. By identifying the phase lag between these quantities, we aim to measure the characteristic timescale associated with feedback-driven clearing of neutral gas in the ISM, consistent with the quasi-cyclic evolution identified in the phase-space and polar analysis.

To compute these time lags we employ the SUNKIT-IMAGE package, part of the SUNPY ecosystem, which provides tools for time-lag and cross-correlation analysis originally developed for solar data. In addition, we independently evaluate cross-correlations using the Pearson correlation coefficient which provides additional robustness to the analysis.

The Pearson correlation coefficient (r) quantifies the strength and direction of the linear relationship between two variables and is defined as

$$r = \frac{\sum_{i=1}^{n}(x_i - \bar{x})(y_i - \bar{y})}{\sqrt{\sum_{i=1}^{n}(x_i - \bar{x})^2}\sqrt{\sum_{i=1}^{n}(y_i - \bar{y})^2}}, \tag{3.5}$$

where x_i and y_i represent the paired measurements and $\bar{x}$ and $\bar{y}$ denote their respective means. The coefficient ranges from -1 to 1, where $r = 1$ indicates a perfect positive correlation, $r = -1$ indicates a perfect negative correlation, and $r = 0$ implies no linear correlation.

When applied to the sSFR and LyC escape fraction time series, the cross-correlation measures how strongly the two quantities are related as a function of temporal offset. Since bursts in star formation are expected to precede peaks in LyC escape, we anticipate a positive time lag. However, the simulation outputs are sampled at irregular intervals across cosmic time, and the data can contain stochastic fluctuations that may produce spurious correlation peaks, which can introduce secondary peaks at larger time lags that do not correspond to the primary physical response.

Because of this we define the lag to be the positive time lag (since physically we know that LyC radiation escape is a delayed response to star formation) corresponding to the first prominent peak in the cross-correlation plot. For which we implement a custom peak-selection algorithm that identifies the first prominent peak corresponding to a positive correlation and the smallest positive lag. This ensures that we get the earliest response of the feedback-driven clearing of surrounding gas, which creates the low-density channels leading to peaks in LyC escape fraction after the sSFR.

Figure 3.10a and Figure 3.10b show the cross-correlation analysis for halo B4, one of the most massive systems in the sample. Both methods yield a characteristic lag of approximately 15 Myr, indicating that the LyC escape fraction peaks roughly 15 Myr after the burstiness parameter peaks. This delay corresponds to the timescale required for stellar feedback to clear dense gas from the star-forming regions and create escape channels for ionising radiation.

The measured lag for halo B4 (~ 15 Myr) is significantly shorter than the cycle timescale inferred from the polar analysis (~ 161 Myr). This difference reflects the fact that the lag traces the local timescale for feedback-driven clearing of the ISM, whereas the polar cycle represents

the longer timescale associated with global gas accretion and starburst recurrence.

To explore how this delay depends on galaxy properties, we repeat the analysis for all halos in the simulation suite and examine the relationship between the measured time lag and halo mass.

			Sunkit		Pearson	
Halo	**Resolution**	**Alias**	**Lag [Myr]**	**Max Corr.**	**Lag [Myr]**	**Max Corr.**
g39	z4	B	15.1	0.44	15.1	0.44
g205	z4	C	12.3	0.61	12.3	0.61
g578	z4	D	36.8	0.40	36.8	0.40
g1163	z4	E	57	0.20	57	0.20
g5760	z4	F	40.5	0.24	43.2	0.34
g5760	z8	F	51.8	0.24	51.8	0.25
g10304	z4	G	18	0.24	18.9	0.25
g10304	z8	G	238.1	0.17	239	0.19
g33206	z4	H	78.7	0.09	78.7	0.18
g33206	z8	H	176.6	0.1	176.6	0.11
g37591	z4	I	108.8	0.06	–	0.06
g37591	z8	I	90.9	0.16	142.6	0.31
g137030	z4	J	125.2	0.15	170.8	0.45
g137030	z8	J	91.6	0.17	91.6	0.17
g137030	z16	J	46	0.29	47.8	0.32
g500531	z4	K	286	0.03	485.2	0.2
g500531	z8	K	103.7	0.2	103.7	0.21
g500531	z16	K	74.8	0.2	74.8	0.2
g519761	z4	L	127.4	0.1	127.4	0.11
g519761	z8	L	107	0.18	107	0.23
g519761	z16	L	427.6	0.1	426.9	0.11
g2274036	z4	M	–	–	–	–
g2274036	z8	M	426.8	0.05	426.8	0.03
g2274036	z16	M	645.8	0.03	645.8	0.13
g5229300	z4	N	29	0.03	321.1	0.04
g5229300	z8	N	156.7	0.01	157.7	0.06
g5229300	z16	N	121.7	0.05	127.5	0.16

Table 3.1: Time lag and correlation strength between sSFR and $f_{\mathrm{esc,LyC}}$ for all halos using SUNKIT-IMAGE and Pearson cross-correlation methods.

The results reveal a trend in which the time lag decreases with increase in halo mass. An the underlying trend is irrespective of the method being used as sunkit or Pearson. For most of the halos and resolution both the methods result in similar time lag and cross correlation, suggesting that the lag and the analysis is robust. However, there are a few outliers to this trend which are resulted by the interpolation scheme and the peak-finding algorithm. The cross-correlation against time lags, for our case result in an oscillatory function with variable amplitudes. As a result, some outliers might be caused by the custom peak-identification logic we have devised.

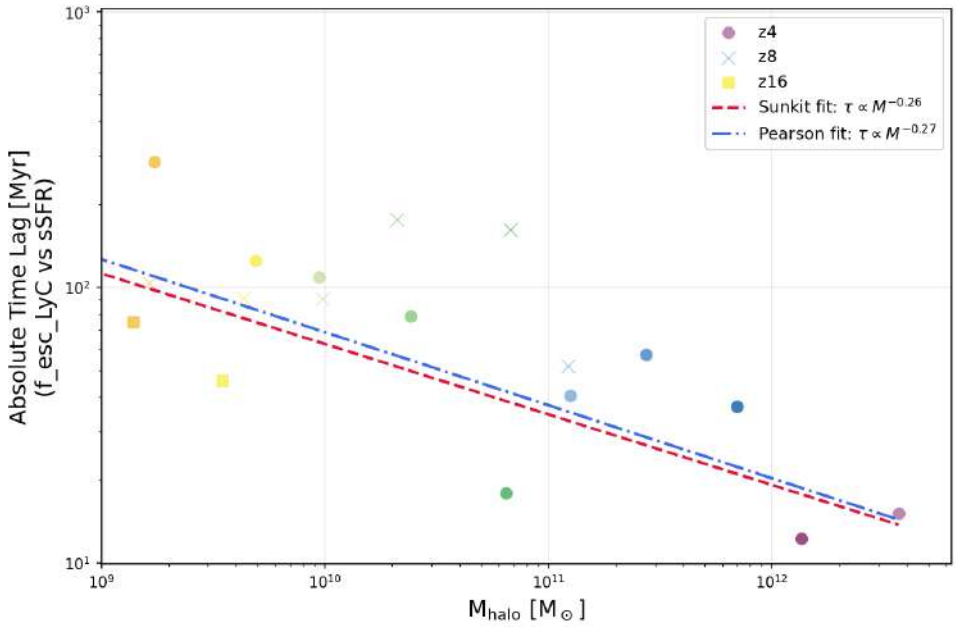

(a) Dependence of the measured time lag between sSFR and $f_{\mathrm{esc,LyC}}$ on halo mass.

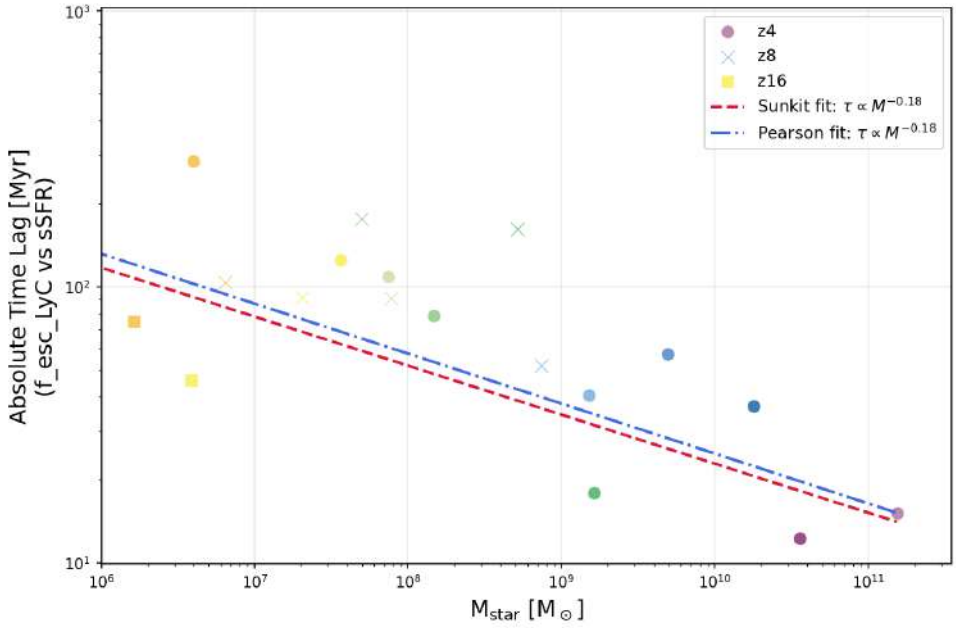

(b) Dependence of the measured time lag on stellar mass.

Figure 3.11: Time-lag measurements for all simulated halos as a function of halo and stellar mass.

The resulting scaling relations with sunkit-correlation weighting can be expressed as

$$\mathrm{lag}^{\mathrm{sSFR}}_{f_{\mathrm{esc,LyC}}} \propto M_{\star}^{-0.18} \qquad \text{and} \qquad \mathrm{lag}^{\mathrm{sSFR}}_{f_{\mathrm{esc,LyC}}} \propto M_{\mathrm{halo}}^{-0.26}. \tag{3.6}$$

Similarly, the scaling relations with Pearson-correlation weighting can be expressed as-

$$\mathrm{lag}^{\mathrm{sSFR}}_{f_{\mathrm{esc,LyC}}} \propto M_{\star}^{-0.18} \qquad \text{and} \qquad \mathrm{lag}^{\mathrm{sSFR}}_{f_{\mathrm{esc,LyC}}} \propto M_{\mathrm{halo}}^{-0.27}. \tag{3.7}$$

In massive halos, because of high gravitational potential and gas accumulation, the starbursts produce more number of stars leading to much stronger feedback events, which results the LyC to peak quickly. As the mass decreases, because of the shallow gravitational potential, the feedback requires more time to adjust to the starburst and affect the ISM, which increases the time lag between sSFR and LyC escape fraction.

The correlation is strongest in massive halos, where feedback-driven cycles are well regulated by the gravitational potential. In low-mass halos, star formation is more bursty and irregular, with longer intervals between star-forming episodes. Stellar feedback can more efficiently expel gas due to the shallow gravitational potential, resulting in a highly porous ISM. Consequently, the escape fraction becomes less tightly coupled to short-timescale variations in star formation, leading to weaker and more irregular cross-correlation signals and less well-defined lag measurements.

We can see from the Table 3.1 that the correlation strength lies in the range 0.2–0.6 for high mass halos and it goes down with the halo mass. The moderate correlation strength indicates that while the escape fraction is influenced by star formation activity, the relationship is not strictly deterministic and is modulated by the complex structure of the ISM.

Overall, these results demonstrate that the escape of ionising radiation is governed by a delayed, feedback-driven response to star formation activity, with the delay representing the timescale over which stellar feedback restructures the ISM.

3.6 Lag with Other Physical Quantities

In the previous section, we established that the evolution of the escape fraction ($f_{\mathrm{esc,LyC}}$) exhibits a measurable lag with respect to the burstiness parameter, leading to quasi-cyclic behaviour in phase space. We now extend this analysis to other physical quantities associated with star formation and Lyman continuum (LyC) radiation in order to determine whether similar delayed responses are present more generally.

The quantities listed in Table 3.2 can be grouped into two physically distinct categories. The intrinsic production rate of ionizing photons, $\dot{N}^{\mathrm{int}}_{\mathrm{LyC}}$, is directly determined by the population of young massive stars and therefore closely traces recent star formation activity, as quantified by SFR_{10}. In contrast, the escaping photon rate $\dot{N}^{\mathrm{esc}}_{\mathrm{LyC}}$ and the escape fraction $f_{\mathrm{esc,LyC}}$ depend not

Table 3.2: Physical quantities related to star formation activity and their connection to Lyman continuum production and escape.

Star Formation Quantities	**LyC-related Quantities**
SFR_{10}	$\dot{N}_{\mathrm{LyC}}^{\mathrm{int}}$
SFR_{100}	$\dot{N}_{\mathrm{LyC}}^{\mathrm{esc}}$
$\frac{\mathrm{SFR}_{10}}{\mathrm{SFR}_{100}}$ or sSFR	$f_{\mathrm{esc,LyC}} \equiv \dot{N}_{\mathrm{LyC}}^{\mathrm{esc}} / \dot{N}_{\mathrm{LyC}}^{\mathrm{int}}$

only on photon production but also on the structure and evolution of the surrounding gas, which regulates the transmission of radiation through the interstellar medium.

We apply the lag analysis described previously to all combinations of star formation and LyC-related quantities in order to identify systematic temporal offsets between production and escape. As expected, quantities that are directly linked to the source population, such as SFR_{10} and $\dot{N}_{\mathrm{LyC}}^{\mathrm{int}}$, exhibit little or no measurable lag, reflecting the prompt response of photon production to changes in star formation. In contrast, quantities involving the escape of radiation, particularly $f_{\mathrm{esc,LyC}}$, show a delayed response relative to star formation indicators, consistent with the time required for stellar feedback to restructure the gas and create low-density channels through which ionizing photons can escape.

Having already examined the lag between $f_{\mathrm{esc,LyC}}$ and the burstiness parameter, we now focus on the remaining combinations in order to further isolate the roles of source variability and feedback-regulated escape in shaping the temporal behaviour of LyC radiation.

3.6.1 Photon Emission vs. Star Formation Rates

We first examine the temporal relationship between star formation rates and LyC photon production and escape. For the set of parameter combinations

$$\left\{\dot{N}_{\mathrm{LyC}}^{\mathrm{int}}, \dot{N}_{\mathrm{LyC}}^{\mathrm{esc}}\right\} \times \left\{\mathrm{SFR}_{10}, \mathrm{SFR}_{100}\right\},$$

we find that all pairs exhibit negligible time lag ($< 5\,\mathrm{Myr}$) across the halo sample, along with strong cross-correlation coefficients in the range 0.6–0.8.

This result indicates that both the intrinsic photon production rate, $\dot{N}_{\mathrm{LyC}}^{\mathrm{int}}$, and the escaping photon rate, $\dot{N}_{\mathrm{LyC}}^{\mathrm{esc}}$, closely follow the time variability of star formation. This behaviour is expected, as $\dot{N}_{\mathrm{LyC}}^{\mathrm{int}}$ is directly determined by the population of young massive stars. The strong correlation between $\dot{N}_{\mathrm{LyC}}^{\mathrm{esc}}$ and star formation arises because the escaping photon rate inherits the variability of the intrinsic source population, with

$$\dot{N}_{\mathrm{LyC}}^{\mathrm{esc}} = f_{\mathrm{esc}} \times \dot{N}_{\mathrm{LyC}}^{\mathrm{int}}.$$

We further find that both $\dot{N}_{\mathrm{LyC}}^{\mathrm{int}}$ and $\dot{N}_{\mathrm{LyC}}^{\mathrm{esc}}$ exhibit a stronger correlation with SFR_{10} compared to SFR_{100}. This reflects the fact that LyC production is dominated by short-lived massive stars,

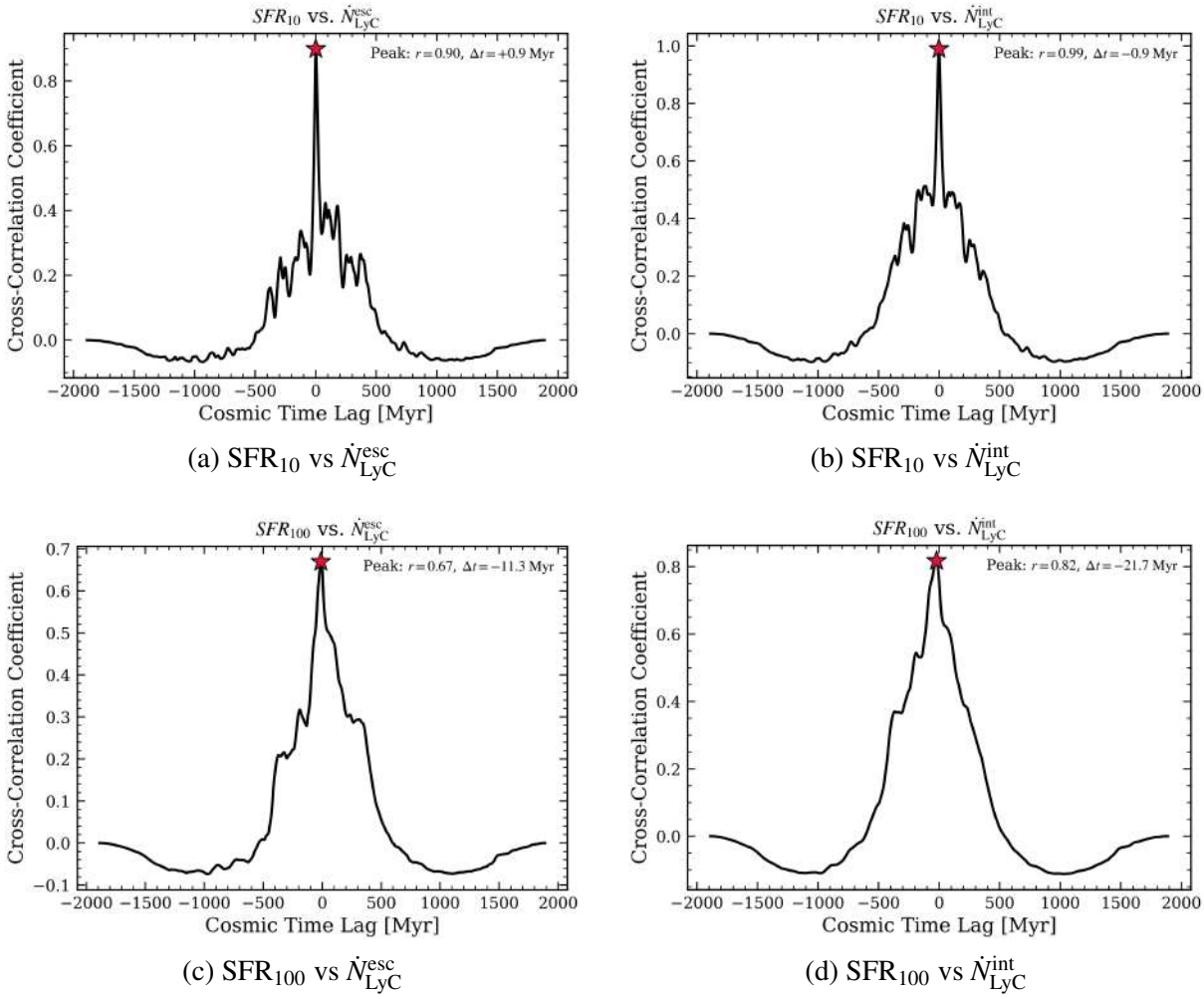

(a) SFR_{10} vs $\dot{N}_{\rm LyC}^{\rm esc}$

(b) SFR_{10} vs $\dot{N}_{\rm LyC}^{\rm int}$

(c) SFR_{100} vs $\dot{N}_{\rm LyC}^{\rm esc}$

(d) SFR_{100} vs $\dot{N}_{\rm LyC}^{\rm int}$

Figure 3.12: Cross-correlation analysis between star formation rates averaged over different timescales (SFR_{10} and SFR_{100}) and LyC photon production and escape rates.

making it more sensitive to recent star formation activity than to longer-term averaged star formation rates.

Overall, these results demonstrate that the production and amplitude of escaping LyC radiation are primarily source-driven, with little or no measurable delay relative to star formation. In contrast, as shown in subsequent sections, the escape fraction $f_{\rm esc}$ exhibits a delayed response, reflecting the role of feedback in regulating photon escape.

3.6.2 Intrinsic and Escaping LyC Photon Emission

We examine the temporal relationship between the intrinsic LyC photon production rate, $\dot{N}_{\rm LyC}^{\rm int}$, and the escaping LyC photon rate, $\dot{N}_{\rm LyC}^{\rm esc}$. Applying the lag analysis pipeline, we find a negligible time lag ($\lesssim 5$ Myr) between the two quantities, along with a strong peak cross-correlation coefficient of ~ 0.8.

The absence of a significant lag indicates that the escape of LyC photons responds almost instantaneously to changes in their production rate. The high cross-correlation depicted in Figure

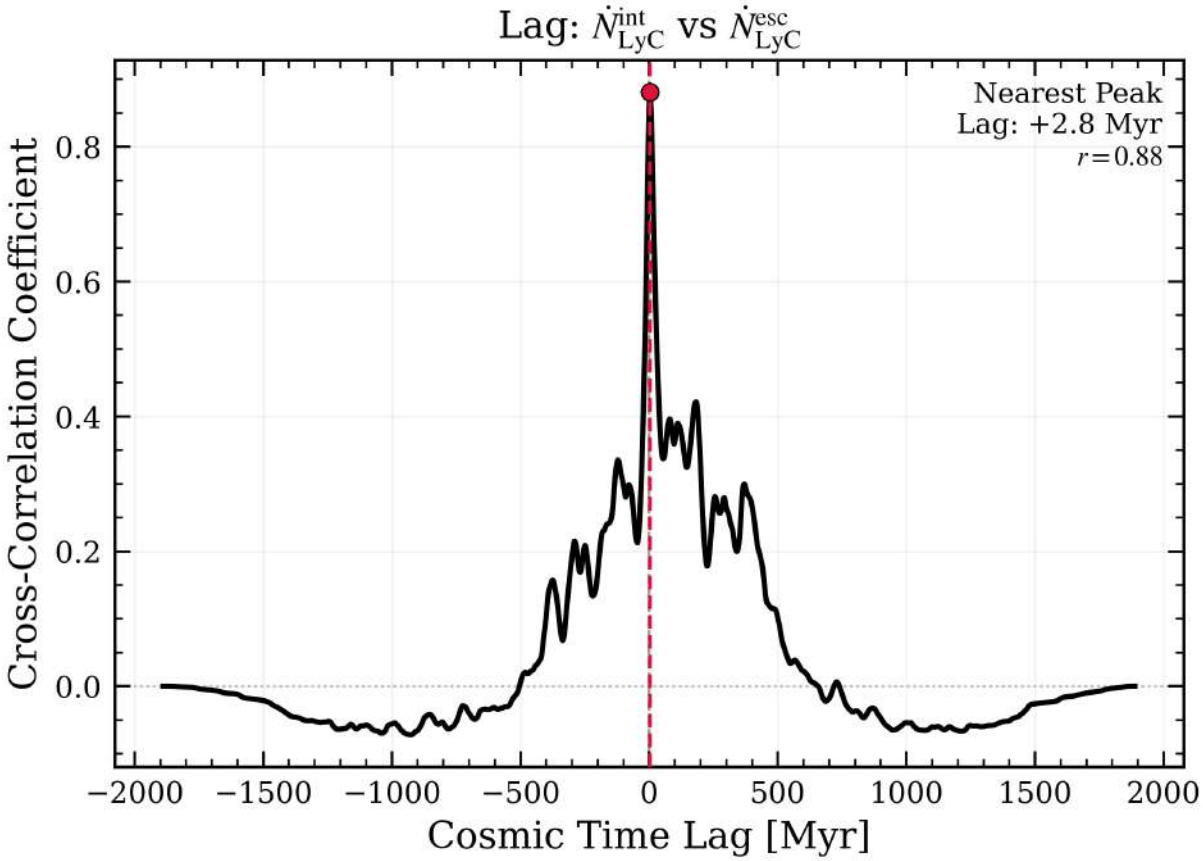

Figure 3.13: Temporal cross-correlation between intrinsic LyC photon production ($\dot{N}_{\rm LyC}^{\rm int}$) and escaping LyC photon emission ($\dot{N}_{\rm LyC}^{\rm esc}$)

3.13 further supports this interpretation, demonstrating that the interstellar medium primarily modulates the amplitude of the escaping radiation without substantially altering its temporal evolution. In other words, while gas distribution and feedback processes regulate the fraction of photons that escape, they do not significantly decouple the escaping emission from the underlying star formation activity on the timescales probed here.

3.6.3 Photon emission vs Burstiness parameter

Despite the peak of the cross-correlation occurring at near-zero lag, the correlation amplitude remains low (~ 0.2), even for high-mass halos where feedback-driven cycles are expected to be more pronounced. This indicates that, although any response between the burstiness parameter and LyC photon emission occurs at an extremely small lag, the coupling between these quantities is intrinsically weak.

Consequently, the absence of a measurable lag does not imply a meaningful physical connection. In particular, variations in burstiness do not provide predictive information about the behaviour of either the intrinsic or escaping LyC photon emission, and vice versa. Therefore, burstiness alone is not a reliable tracer of LyC photon production or escape.

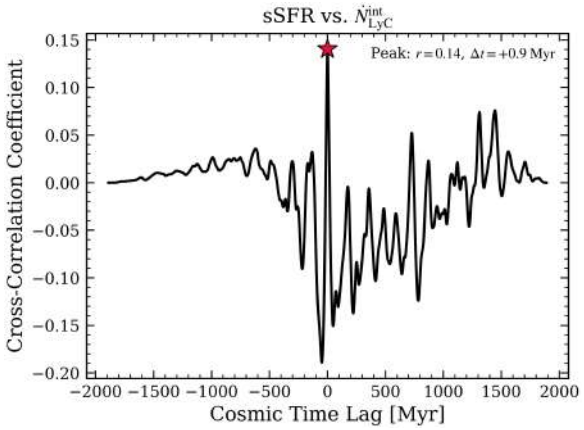

(a) sSFR vs $\dot{N}_{\rm LyC}^{\rm int}$

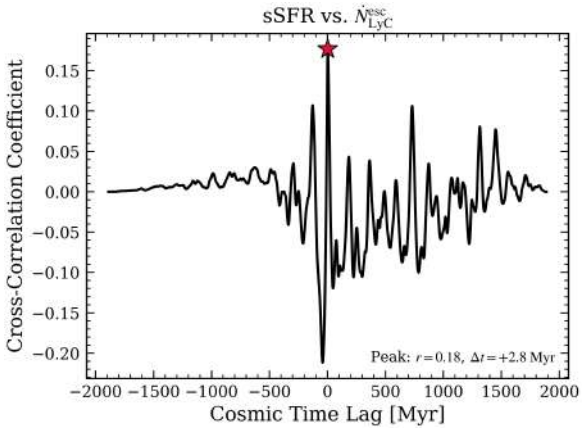

(b) sSFR vs $\dot{N}_{\rm LyC}^{\rm esc}$

Figure 3.14: Temporal cross-correlation between sSFR and intrinsic LyC photon production ($\dot{N}_{\rm LyC}^{\rm int}$) and escaping LyC photon emission ($\dot{N}_{\rm LyC}^{\rm esc}$)

3.6.4 Escape fraction vs Star Formation

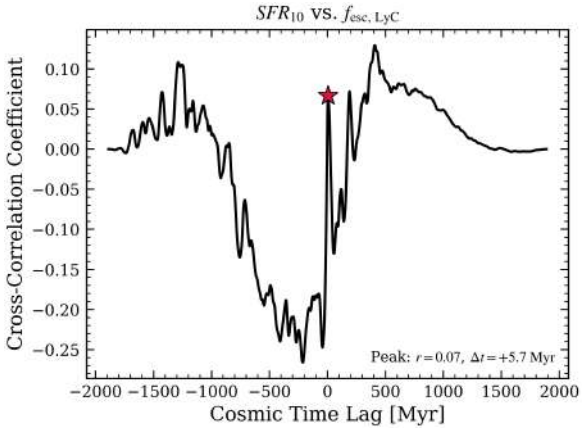

(a) Cross-correlation between SFR_{10} and LyC escape fraction, $f_{\rm esc,LyC}$.

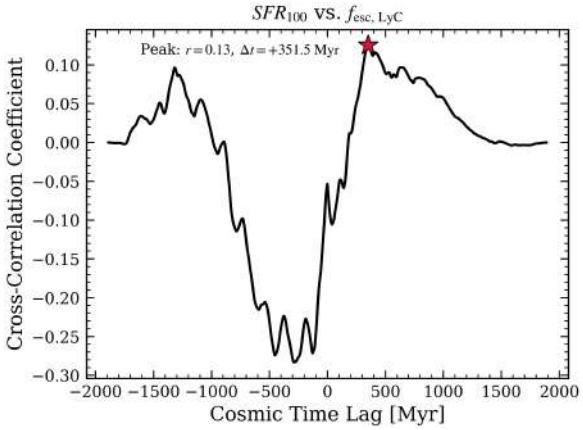

(b) Cross-correlation between SFR_{100} and LyC escape fraction, $f_{\rm esc,LyC}$.

Figure 3.15: Temporal cross-correlation between star formation rates on different timescales and the LyC escape fraction.

We now examine the relationship between the LyC escape fraction and star formation rates on different timescales. As shown in Figure 3.15, both SFR_{10} and SFR_{100} exhibit weak cross-correlation with $f_{\rm esc,LyC}$, particularly in high-mass halos.

While the cross-correlation functions may show indications of a preferred lag, the amplitude of the correlation remains low, suggesting that any apparent temporal offset is not statistically significant. Therefore, neither SFR_{10} nor SFR_{100} provides strong predictive power for the behaviour of the escape fraction.

Physically, this reflects the fact that the escape of LyC photons is not governed solely by the rate of star formation, but is instead regulated by the structure and evolution of the surrounding interstellar medium. While star formation sets the supply of ionizing photons, the escape frac-

tion depends on the presence of low-density channels, which are shaped by feedback processes and gas dynamics.

Consequently, variations in star formation rate do not directly translate into variations in escape fraction, leading to a weak overall coupling between these quantities.

3.6.5 Physical Picture

Combining the results from the time-lag and cross-correlation analyses, we arrive at a coherent physical picture linking star formation, feedback, and LyC radiation escape.

We find that the LyC escape fraction, $f_{\mathrm{esc,LyC}}$, exhibits a measurable lag with respect to the burstiness parameter, with a moderate correlation that is most prominent in high-mass halos. This behaviour suggests that the escape of ionizing radiation is regulated by feedback processes that act to restructure the surrounding interstellar medium. In these systems, episodes of enhanced star formation drive feedback that disrupts dense gas and carves low-density channels, enabling a larger fraction of LyC photons to escape after a finite delay.

In contrast, the strength of this correlation decreases toward lower-mass halos. Due to their shallower gravitational potentials, gas can be more easily removed or redistributed, leading to consistently low column densities. As a result, the escape fraction can remain high irrespective of the recent star formation history, producing a weak or negligible correlation with the burstiness parameter.

On the other hand, both the intrinsic and escaping LyC photon emission rates show negligible lag and strong correlation with star formation. This reflects the fact that LyC photons are produced by young, massive stars, and therefore track the star formation rate almost instantaneously.

Taken together, these results highlight a clear separation of roles. Star formation directly controls the *production* of LyC photons, while feedback-driven restructuring of the interstellar medium governs their *escape*. The burstiness parameter, as a measure of short-term variability in star formation, is therefore more closely linked to the timing of feedback processes than to the absolute photon production rate.

This explains the quasi-cycle we observed in previous section, where following a starburst, LyC photon production increases immediately, but the surrounding medium remains optically thick. Only after feedback processes act to clear or redistribute the gas do low-density channels form, allowing LyC photons to escape. The escape fraction thus rises with a delay relative to the burstiness parameter, giving rise to the quasi-cyclic behaviour observed in phase space.

3.6.6 Observational Signature

The analysis presented in the previous sections relies on quantities such as SFR_{10} and SFR_{100}, which are not directly observable but are instead inferred from spectral diagnostics. To con-

nect our results to observable quantities, we construct an empirical proxy for the burstiness parameter using widely used star formation tracers.

The Hα luminosity traces recent star formation on timescales of $\sim 10\,\mathrm{Myr}$, while the ultraviolet continuum luminosity (e.g., L_{1500}) probes star formation averaged over longer timescales of $\sim 100\,\mathrm{Myr}$ [10]. Motivated by this, we define an observational signature (OS) as

$$\mathrm{OS} = \frac{L_{\mathrm{H}\alpha}}{L_{1500}}\,, \tag{3.8}$$

which serves as an observable analogue of the burstiness parameter.

We apply the same temporal lag and cross-correlation analysis between this observational signature and the LyC escape fraction. The resulting cross-correlation function for a representative halo (B4) is shown in Figure 3.16. We find that the observational signature reproduces the key behaviour seen with the burstiness parameter, exhibiting a prominent peak at a positive time lag. This indicates that the delay between star formation variability and LyC escape is preserved even when using observational proxies.

Extending this analysis to the full halo sample, we measure the lag as a function of stellar mass ($M_\star$) and halo mass (M_{halo}). In both cases, the lag exhibits a clear scaling with mass, which can be described by power-law relations of the form

$$\mathrm{lag}^{\mathrm{OS}}_{f_{\mathrm{esc,LyC}}} \propto M_\star^{-0.20} \qquad \text{and} \qquad \mathrm{lag}^{\mathrm{OS}}_{f_{\mathrm{esc,LyC}}} \propto M_{\mathrm{halo}}^{-0.30}\,. \tag{3.9}$$

These scaling relations are consistent with those obtained using the intrinsic burstiness parameter, demonstrating that the underlying physical connection between star formation variability, feedback, and LyC escape can be recovered using observable quantities. This demonstrates that the delayed response of LyC escape to star formation variability is not only a robust physical feature of the simulations, but also a directly testable prediction for observations of high-redshift galaxies.

3.7 Peak and Trough Analysis

To further investigate the cyclic behaviour identified in the time-lag analysis, we perform a peak and trough analysis on the time-series data of key physical quantities such as the LyC escape fraction ($f_{\mathrm{esc,LyC}}$), the burstiness parameter (sSFR), and the star formation rate averaged over short timescales (SFR_{10}). These quantities exhibit characteristic burst and quenching phases that can be identified through their local maxima and minima.

In order to robustly identify these features in noisy simulation data, we implement a custom peak-detection algorithm. Similar to the approach used in the cross-correlation analysis, this algorithm searches for prominent peaks and troughs within the time series while suppressing small-amplitude fluctuations that arise from numerical noise or minor stochastic variations.

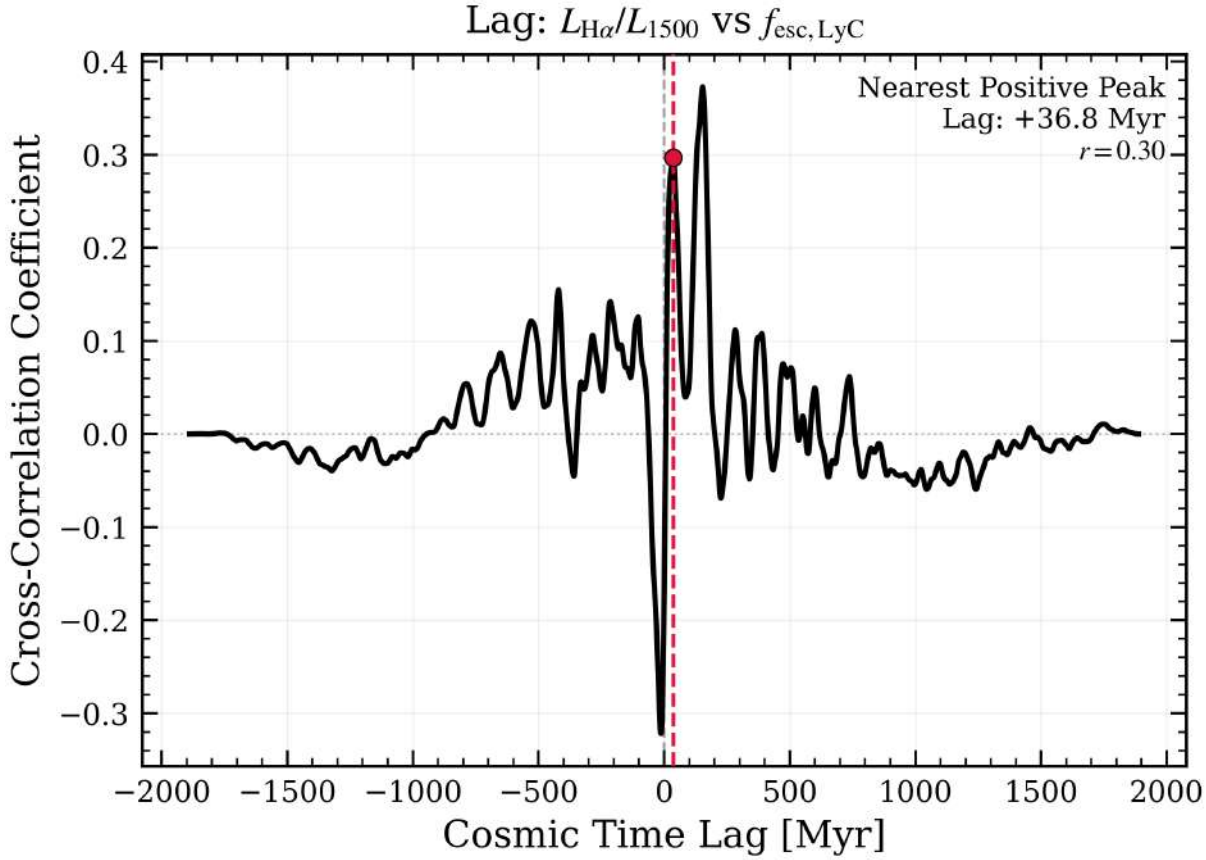

Figure 3.16: Temporal cross-correlation between the observational signature ($L_{H\alpha}/L_{1500}$) and the LyC escape fraction

A peak is classified as a prominent burst only if its amplitude exceeds that of neighbouring peaks by a specified logarithmic threshold. In this work, we apply masks corresponding to peak separations of 0.25, 0.5, or 1 dex in order to isolate physically significant burst events. Once a peak is identified, the corresponding trough is defined as the minimum value attained by the signal between two consecutive peaks. Conversely, peaks are required to represent the maximum value between two neighbouring troughs. The indices of these peaks and troughs are stored and subsequently used to analyse the temporal evolution of starburst cycles.

An example of the peak and trough identification applied to the time series is shown in Figures 3.19 and 3.18, where the detected extrema are overlaid on the original signal.

3.7.1 Persistence Plots

To further quantify the cyclic nature of star formation and LyC escape, we apply persistence analysis, a technique originating from Topological Data Analysis (TDA). While traditional peak-finding methods identify local extrema, persistence analysis provides a quantitative measure of the robustness of these features by evaluating how long they persist across the amplitude landscape of the signal.

In this framework, each peak and trough pair is treated as a topological feature. A feature

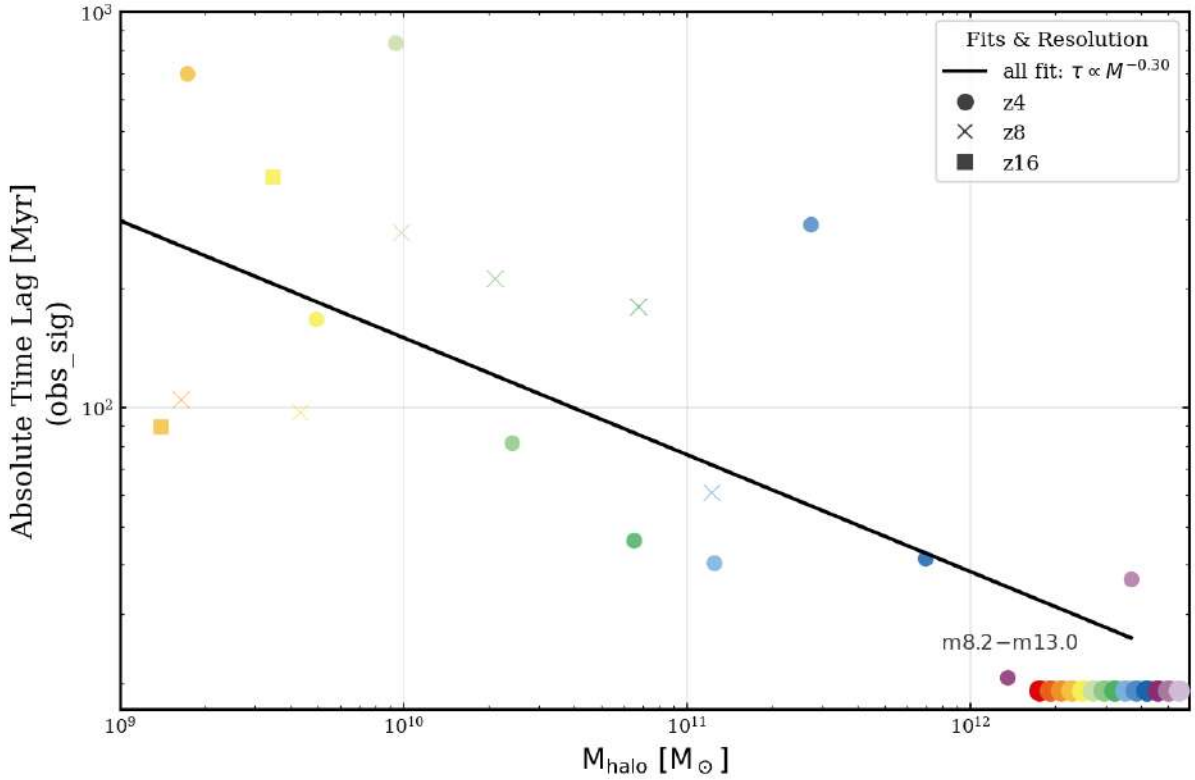

(a) Lag between the observational signature ($L_{H\alpha}/L_{1500}$) and the LyC escape fraction as a function of halo mass, M_{halo}.

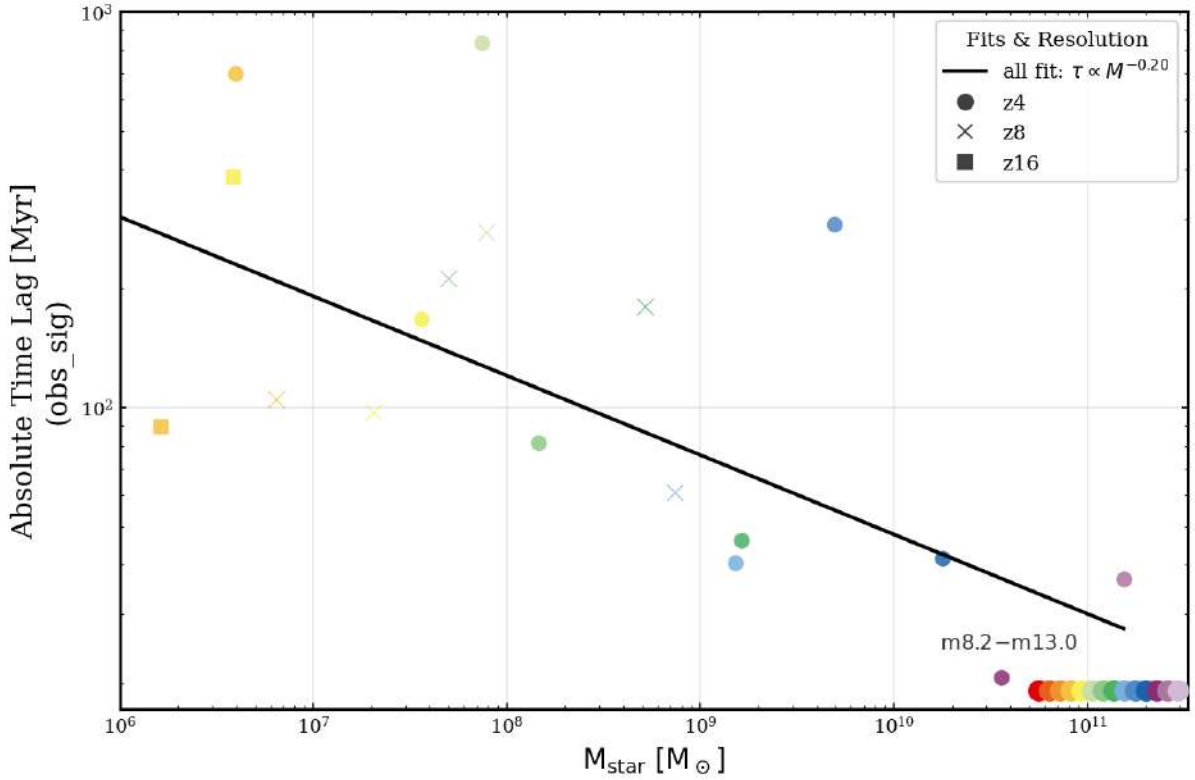

(b) Lag between the observational signature and the LyC escape fraction as a function of stellar mass, $M_\star$.

Figure 3.17: Dependence of the time lag between the observational signature ($L_{H\alpha}/L_{1500}$) and the LyC escape fraction on halo mass (top) and stellar mass (bottom).

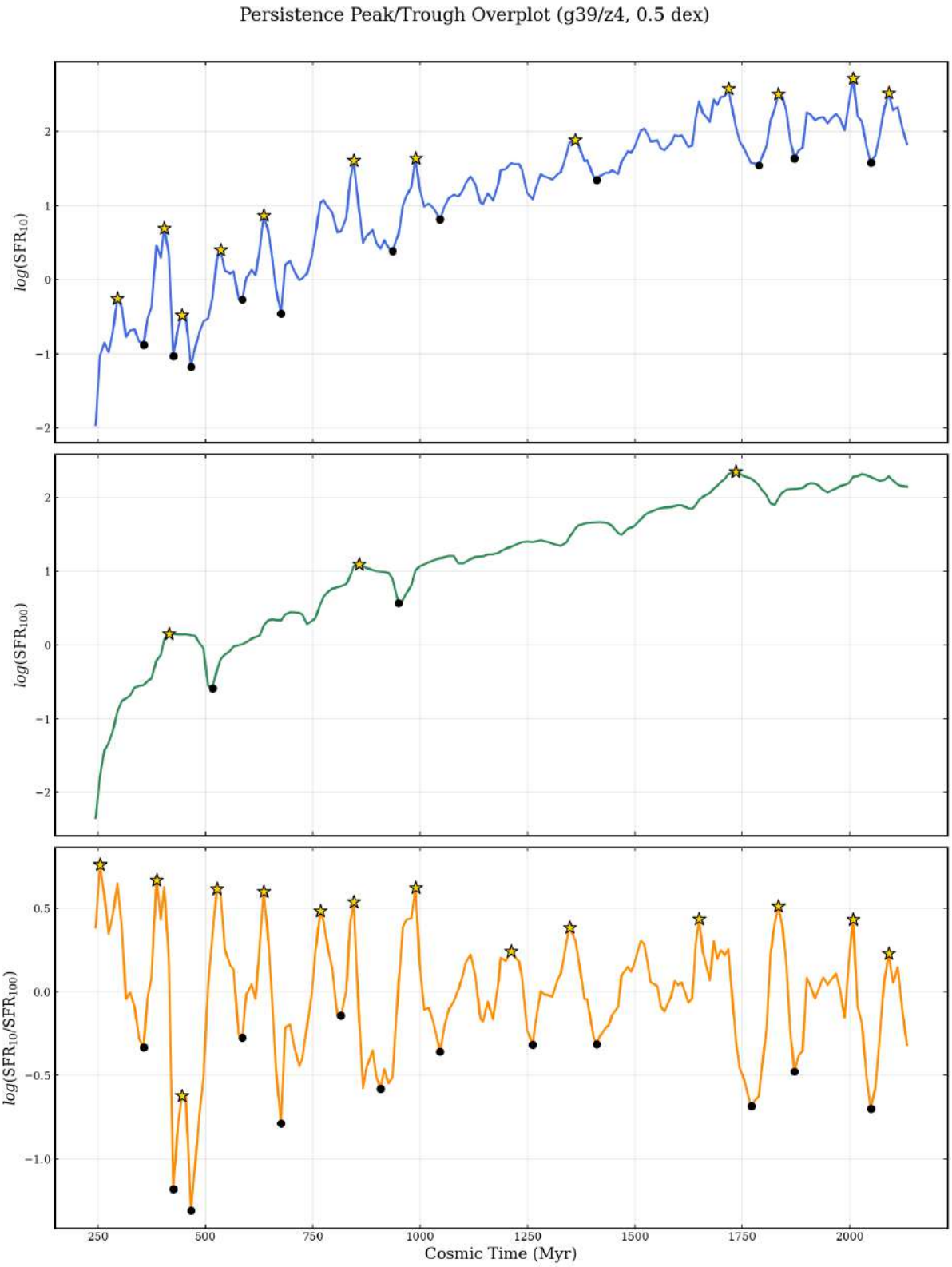

Figure 3.18: Peak and Trough overplot for $\log(\mathrm{SFR}_{10})$, $\log(\mathrm{SFR}_{100})$, and $\log(\mathrm{sSFR})$.

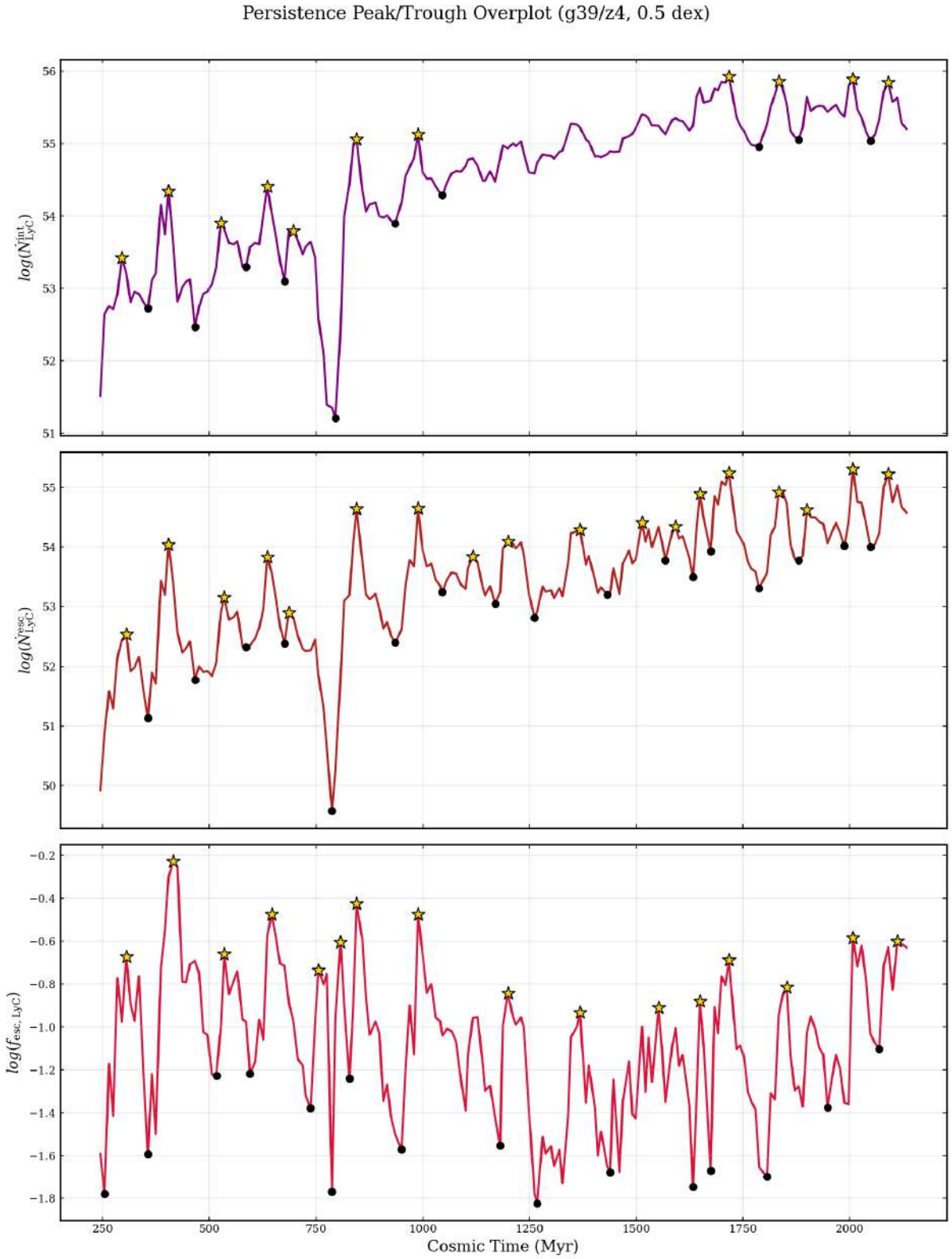

Figure 3.19: Peak and Trough overplot for $\log(\dot{N}_{\mathrm{LyC}}^{\mathrm{int}})$, $\log(\dot{N}_{\mathrm{LyC}}^{\mathrm{esc}})$, and $\log(f_{\mathrm{esc,\,LyC}})$.

is considered to be "born" at a local minimum (trough) and to "die" at the corresponding local maximum (peak). The persistence of the feature is defined as the difference between these values:

$$P = |V_{\text{death}} - V_{\text{birth}}| \,. \tag{3.10}$$

A persistence diagram plots the birth value on the horizontal axis and the death value on the vertical axis. Features located far from the diagonal ($x = y$) have large persistence and correspond to dominant physical cycles, whereas points located near the diagonal represent small-amplitude fluctuations that are typically associated with noise.

The persistence diagrams reveal distinct topological signatures for different physical quantities, reflecting the underlying mechanisms that govern their variability.

- f_{esc} **and sSFR clustering.** The persistence diagrams for the escape fraction and specific star formation rate exhibit clustered distributions of points. In the context of TDA, such clustering indicates that burst events occur over a range of absolute values while maintaining a relatively consistent persistence. This suggests that LyC escape is not a simple binary process but instead depends strongly on the evolving structure of the interstellar medium. The depth of the cycles—corresponding to how strongly the escape fraction resets between bursts—varies depending on the instantaneous geometry of ionized channels and the neutral gas distribution.

- SFR_{10} **and** $\dot{N}_{\text{esc,LyC}}$ **diagonal trend.** In contrast, the persistence diagrams for SFR_{10} and the escaping ionizing photon rate exhibit points distributed approximately along a line parallel to the $y = x$ diagonal. This topology indicates that individual starburst events have similar prominence relative to their local baseline. In other words, while the overall level of star formation may evolve over time, the amplitude of individual burst events remains relatively consistent.

Physically, this behaviour suggests that star formation within the simulated galaxies is governed by a self-regulated feedback cycle. Stellar feedback periodically disrupts the gas reservoir, temporarily suppressing star formation before the system re-accretes gas and enters the next burst phase. This self-regulation leads to starburst episodes with comparable amplitudes even as the global star formation level evolves. In contrast, the LyC escape fraction exhibits more complex behaviour, as it depends sensitively on the instantaneous geometry and column density structure of the interstellar medium, leading to a more scattered persistence distribution.

3.7.2 Peak–Trough Temporal Analysis

Having identified peaks and troughs in the time-evolution of each quantity, we now quantify the characteristic timescale of variability by measuring the time interval between successive peaks. This provides an independent estimate of the cyclic behaviour observed in the lag analysis.

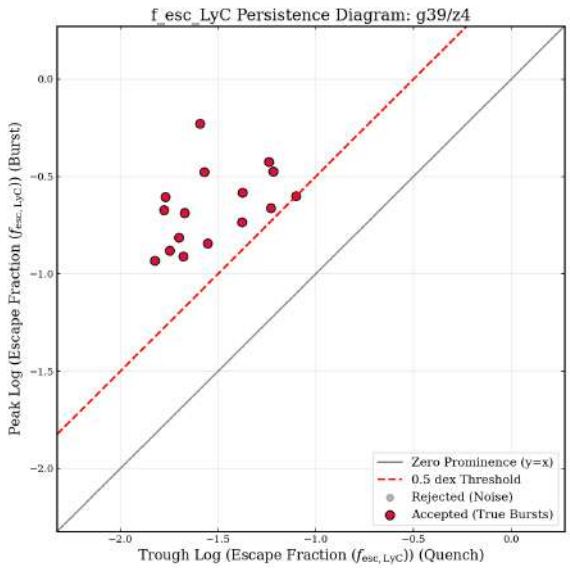

(a) Persistence diagram for $f_{\mathrm{esc,LyC}}$.

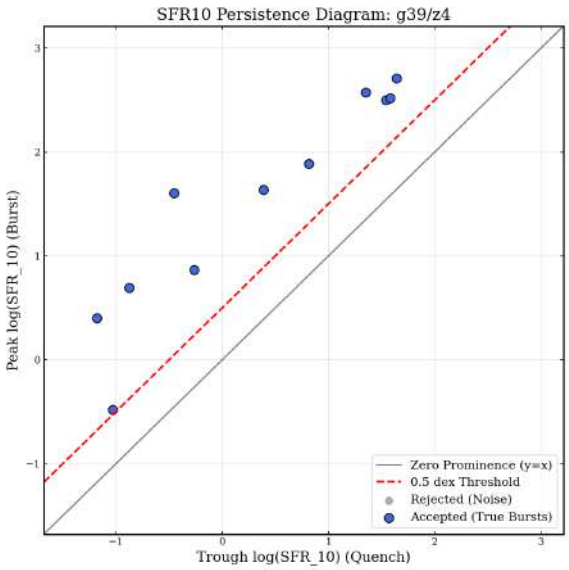

(b) Persistence diagram for SFR_{10}.

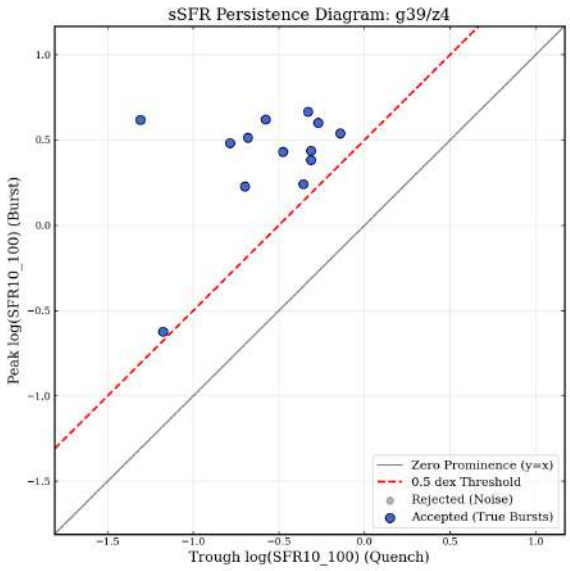

(c) Persistence diagram for sSFR.

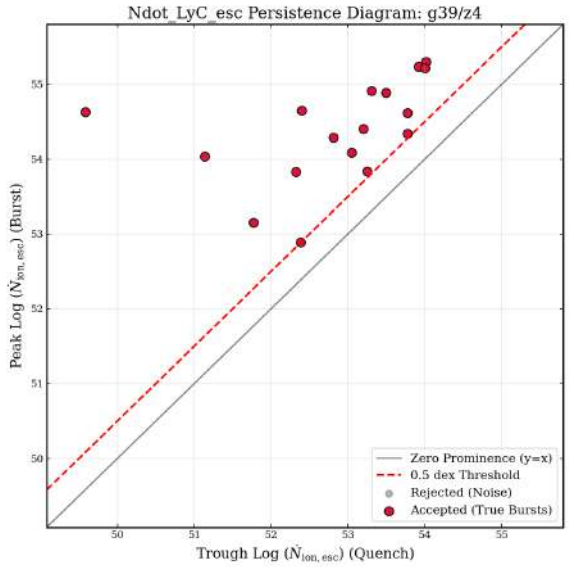

(d) Persistence diagram for escaping LyC photon rate $\dot{N}_{\mathrm{esc,LyC}}$.

Figure 3.20: Persistence diagrams illustrating the topological structure of burst and quenching cycles in various physical parameters.

The identification of peaks and troughs depends on the adopted dex threshold, which determines the minimum prominence required to distinguish physical variability from noise. While a threshold of 0.5 dex is sufficient for most quantities, we explore three values namely, 0.25 (lenient), 0.5 (fiducial), and 1.0 (strict), to assess the robustness of our results. The threshold thus acts as a tunable parameter that can be adapted to different physical quantities.

For each halo, we compute the time between consecutive peaks and associate this timescale with the stellar or halo mass measured at the corresponding trough. The resulting distributions are shown in Figure 3.21. Scatter points correspond to the fiducial threshold (0.5 dex), while the trend lines represent binned averages across all thresholds.

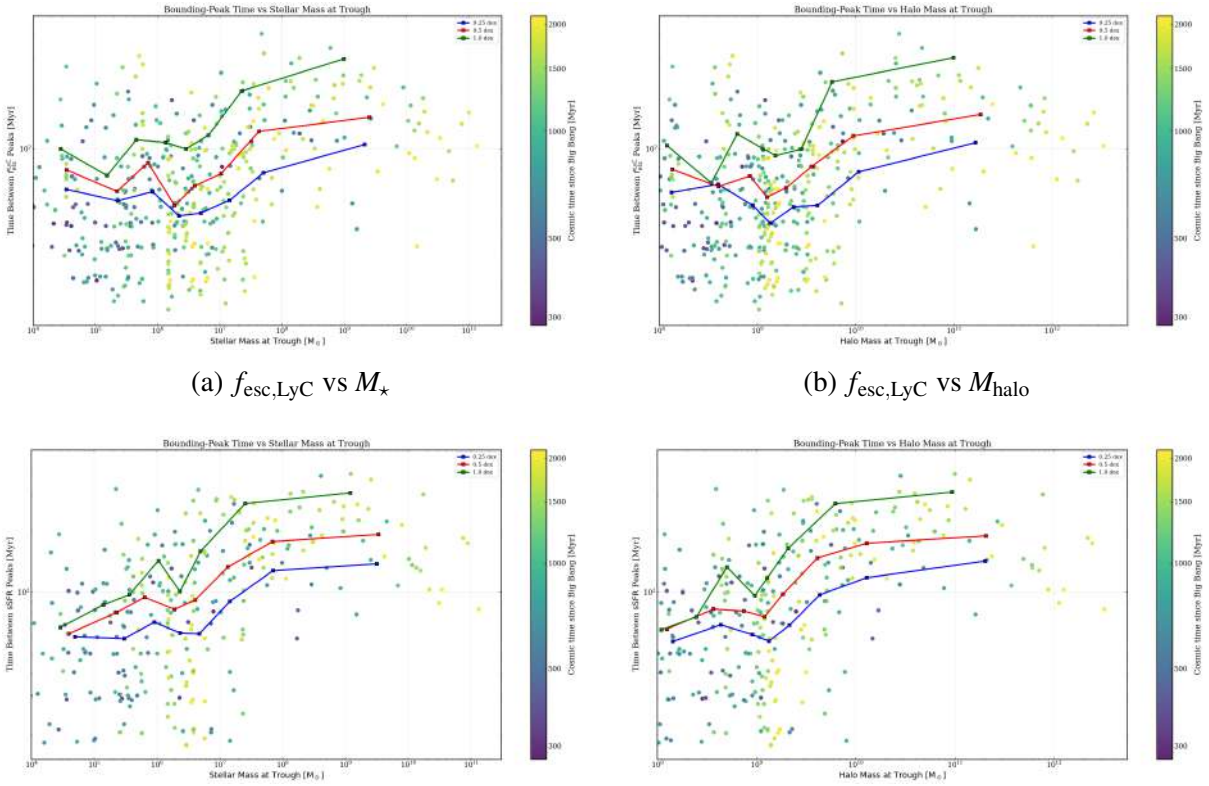

(a) $f_{\mathrm{esc,LyC}}$ vs $M_\star$

(b) $f_{\mathrm{esc,LyC}}$ vs M_{halo}

(c) Burstiness ($\mathrm{SFR}_{10}/\mathrm{SFR}_{100}$) vs $M_\star$

(d) Burstiness ($\mathrm{SFR}_{10}/\mathrm{SFR}_{100}$) vs M_{halo}

Figure 3.21: Time between successive peaks as a function of mass measured at the trough. The left column shows scaling with stellar mass ($M_\star$), while the right column shows scaling with halo mass (M_{halo}). The top row corresponds to the LyC escape fraction, and the bottom row corresponds to the burstiness parameter.

A clear mass-dependent behaviour emerges from these figures. Low-mass halos exhibit significant scatter with no well-defined trend, reflecting their shallow gravitational potentials, which limit their ability to re-accrete gas after feedback-driven outflows. As a result, their evolution is highly stochastic, and no characteristic timescale is established.

In intermediate-mass halos, there is a competition between feedback-driven gas expulsion and gravitational re-accretion. This interplay leads to increased variability and scatter in the peak-to-peak timescales, producing a noisy but structured distribution.

At higher masses, the scatter reduces significantly and the characteristic timescales begin to plateau. In this regime, deeper gravitational potentials retain gas more effectively, enabling a more regular cycle of gas accumulation, star formation, and feedback. This leads to a quasi-periodic behaviour with a well-defined timescale.

3.8 Cycle Variability and Burst Amplitude

After identifying the characteristic cycle timescales and the corresponding peak and trough values of the LyC escape fraction, we quantify the strength of individual escape events using the burst amplitude. We define the burst amplitude as the ratio between the peak and trough values of the escape fraction within a given cycle. A large burst amplitude indicates a strongly intermittent episode, in which the escape fraction changes by several orders of magnitude, whereas a smaller amplitude corresponds to a more regulated cycle with weaker temporal fluctuations.

Figure 3.22a shows the burst amplitude of the LyC escape fraction as a function of halo mass measured at the trough of each cycle. At low halo masses, particularly around $M_{\rm halo} \sim 10^8\,M_\odot$, the burst amplitude spans a very broad range and can reach values of several orders of magnitude. This indicates that low-mass halos undergo highly intermittent LyC escape, where feedback events can temporarily remove the surrounding gas to open extremely high escape channels and produce sharp increases in $f_{\rm esc,LyC}$ relative to its quiescent state. The large scatter in this regime reflects the stochastic nature of feedback and gas clearing in shallow gravitational potentials.

As halo mass increases, the upper envelope of the burst amplitude decreases substantially. Higher-mass halos still exhibit temporal variability in their LyC escape fraction, but the amplitude of these fluctuations is confined to a much narrower range. This suggests that these systems are not completely quiescent, but that their deeper gravitational potentials and more developed gas reservoirs regulate the response of the ISM to stellar feedback. As a result, LyC escape proceeds through more moderate and repeatable cycles rather than through extreme burst-like events.

We further quantify the cycle-to-cycle variability of the escape fraction by computing the standard deviation of $f_{\rm esc,LyC}$ between successive peaks during its temporal evolution. This quantity measures the typical fluctuation strength within an individual escape cycle. However, the stochasticity of the population is more clearly reflected by the spread around the median trend, represented by the 16th–84th percentile range. A broad interquartile range indicates that halos of similar mass can exhibit very different levels of cycle variability, corresponding to highly stochastic and irregular LyC escape behaviour. Conversely, a narrower interquartile range implies that the escape cycles are more consistent across the halo population.

Figure 3.22b shows that low-mass halos exhibit a broad spread around the median trend, indicating that their LyC escape cycles are highly stochastic. In this regime, individual feedback episodes can produce very different levels of gas clearing and LyC leakage, even for halos of

comparable mass. As halo mass increases, the interquartile range becomes more compact, suggesting that the cycle-to-cycle behaviour becomes progressively more regulated. Although the median variability does not show a strictly monotonic decrease with halo mass, the narrowing of the percentile range indicates a reduction in stochasticity. This supports the interpretation that increasing halo mass suppresses the most extreme cycle-to-cycle differences and leads to more coherent feedback-regulated LyC escape.

Overall, this analysis reinforces the picture that the temporal variability of LyC escape is governed by the interplay between stellar feedback and the depth of the gravitational potential. In low-mass halos, feedback can produce large and irregular fluctuations in the escape fraction because the surrounding gas is more easily disrupted. In more massive halos, the response of the ISM is more regulated, leading to escape cycles that remain variable but are less dominated by extreme burst-like events.

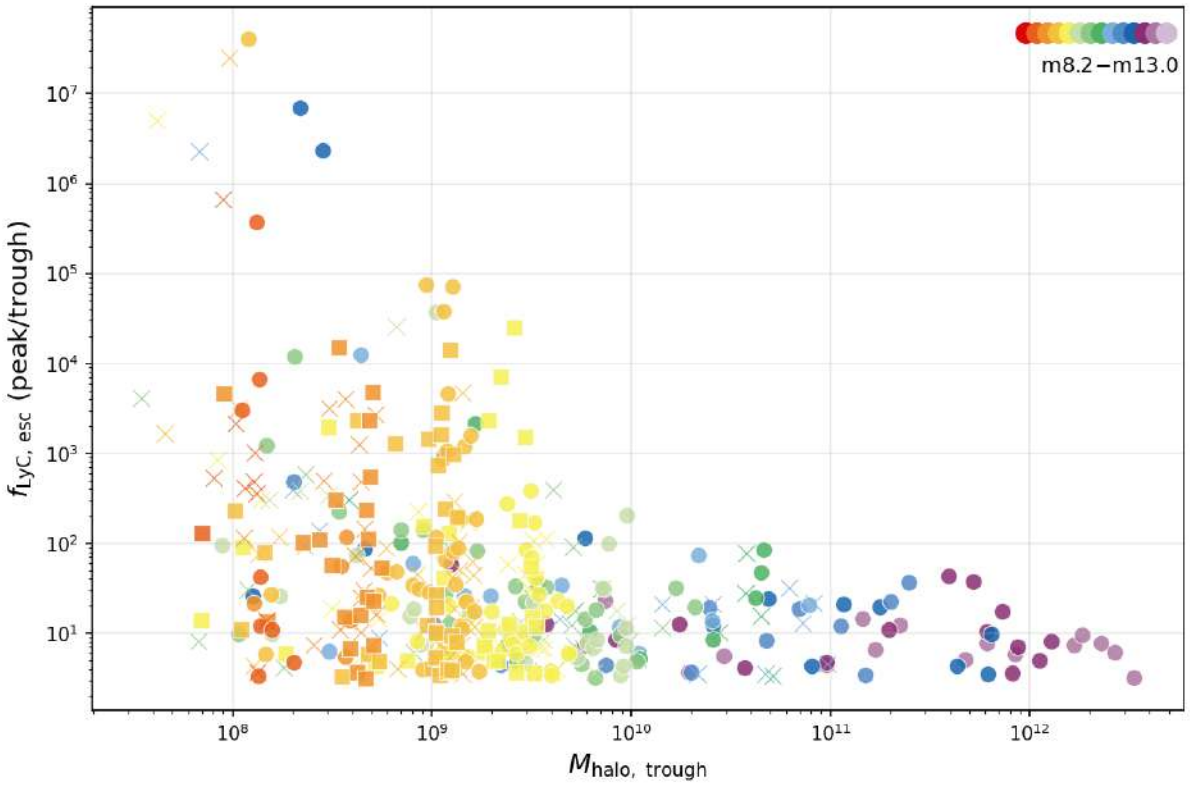

(a) Burst amplitude of the LyC escape fraction, $f_{\mathrm{esc,LyC}}$ as a function of halo mass measured at the trough, $M_{\mathrm{halo,\,trough}}$.

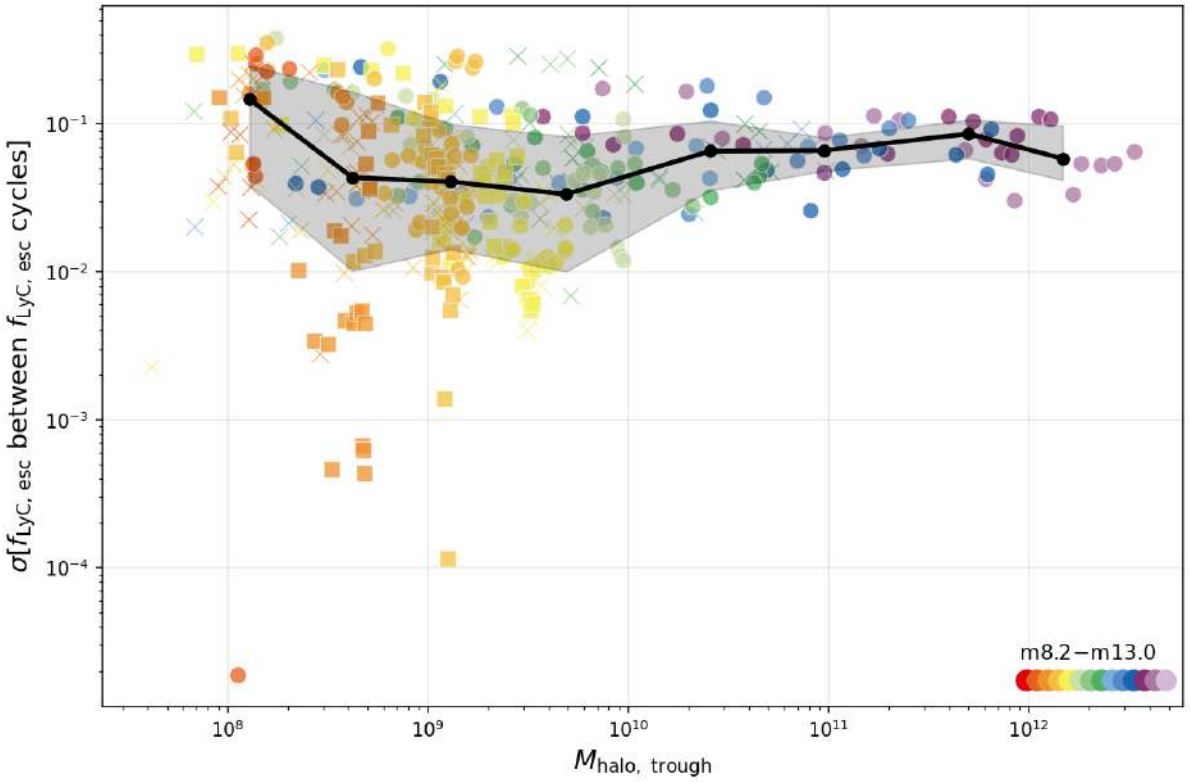

(b) Cycle-to-cycle variability of the LyC escape fraction $f_{\mathrm{esc,LyC}}$ as a function of halo mass measured at the trough, $M_{\mathrm{halo,\,trough}}$. The shaded region shows the 16th–84th percentile range, while the black curve shows the median in each mass bin.

Figure 3.22: Dependence of the burst amplitude (top) and cycle-to-cycle variability (bottom) of the LyC escape fraction, $f_{\mathrm{esc,LyC}}$, on halo mass measured at the trough.

Chapter 4

Conclusion

Understanding the escape of ionizing radiation from galaxies is central to explaining the origin and progression of cosmic reionization. However, direct observations of Lyman Continuum (LyC) radiation are severely limited at high redshift due to absorption by the intergalactic medium. Consequently, identifying robust secondary tracers that can indirectly constrain LyC escape remains a critical challenge in modern astrophysics.

In this work, we investigated the physical mechanisms regulating LyC escape using radiative transfer post-processing performed with COLT on galaxies drawn from the THESAN-ZOOM simulation suite. By combining synthetic observables with time-series analysis of galaxy evolution, we quantify how the escape of ionizing radiation is linked to star formation activity, feedback processes, and the evolving structure of the interstellar medium (ISM).

4.1 Summary of Results

Our analysis began with a population-level exploration of correlations between LyC escape properties and observable galactic tracers. Using two-dimensional phase-space density maps, we quantified statistical relationships between several key parameters and the LyC escape fraction ($f_{\rm esc,LyC}$), as well as the intrinsic and escaping ionizing photon production rates. These parameters are essential in describing LyC leakage from galaxies. Rather than relying on scatter plots, we employed binned median trendlines and interquartile ranges to identify robust global trends while mitigating the influence of stochastic fluctuations inherent in bursty star formation histories, where the slope gives insight in how strongly the two parameters might be correlated, and the scatter and IQR gave insights into the accuracy of it.

Among the explored tracers, quantities related to star formation show the strongest connection to LyC emission and escape. In particular, short-timescale star formation rates ($\rm SFR_{10}$) are strongly correlated with intrinsic LyC photon production, while the burstiness parameter (sSFR) exhibits a moderate correlation with the escape fraction. Physically, starburst episodes increase LyC photon production and inject energy and momentum into the ISM, which subse-

quently creates low-density channels that enable ionizing radiation to escape with a delay.

To further investigate this behaviour, we analyzed the cyclic evolution of these parameters in phase space. By defining a moving centre using a running average over 10 snapshots, we transformed the trajectories into polar coordinates. The unwrapped angular component exhibits an approximately linear trend with time, allowing us to estimate a characteristic cycle period. For high-mass halos, this yields a timescale of $\sim 150\,\mathrm{Myr}$, while lower-mass systems exhibit longer and more irregular cycles, extending up to $\sim 1\,\mathrm{Gyr}$. Short-timescale star formation is not directly observable but can be inferred from tracers such as Hα luminosity. Similarly, longer-timescale star formation (SFR_{100}) can be inferred from ultraviolet indicators such as M_{UV} or L_{1500}.

We also analyze the temporal relationship between star formation activity and LyC escape using time-lag analysis. Cross-correlation methods, including both Fourier-based techniques and Pearson correlation scans, reveal a systematic delay between peaks in star formation activity and the subsequent increase in LyC escape fraction. For the most massive halo in our sample, we measure a characteristic delay of approximately 15 Myr between the burstiness parameter and the escape fraction for high mass halos. This lag corresponds to the timescale required for stellar feedback processes, such as radiation pressure, stellar winds, and supernova explosions, to disrupt dense gas in star-forming regions and open ionized channels within the ISM.

Extending this analysis to the full halo sample reveals that the magnitude of this delay depends on galaxy mass. Massive halos exhibit stronger correlations between star formation and LyC escape and display well-defined time lags, reflecting the cyclic regulation of gas inflow, star formation, and feedback in gravitationally confined systems. In contrast, low-mass halos tend to show weaker correlations and less clearly defined lags, consistent with their shallow gravitational potentials that allow stellar feedback to more efficiently expel gas and maintain a highly porous ISM. This analysis confirms that the escape fraction generally rises after star formation peaks, consistent with the feedback-driven clearing of neutral gas from the ISM.

In order to characterize these cycles more directly, we perform a peak and trough analysis on the time-series data. By identifying prominent maxima and minima in parameters such as $f_{\mathrm{esc,LyC}}$ and sSFR, we isolate individual burst–quenching cycles in the evolutionary history of each galaxy. Finally, we apply persistence analysis from topological data analysis (TDA) to quantify the robustness of these cycles. Persistence diagrams reveal distinct structural differences between star formation indicators and LyC escape properties. Star formation metrics tend to exhibit relatively uniform burst amplitudes, producing persistence features aligned near the diagonal of the persistence plane. In contrast, the escape fraction showed a broader distribution of persistence values, reflecting the complex and highly variable geometry of ionized channels in the ISM. This behaviour highlights the fundamentally stochastic nature of LyC escape compared to the more self-regulated processes governing star formation.

Alongwith the persistance diagrams, we use this peak identification logic to find the peaks

and troughs, and upon calculating the time between the bounding peaks, we find that low mass halos depict high scatter and stochastic noise. As the mass increase, the gravity becomes strong enough to be able to pull back the outflowing gas due to the feedback processes. And once the mass increases beyond a tipping point that the feedback outflows can never escape the gravitational potential, which is the case for high-mass halos, start depicting less scatter and robust trends irrespective of the dex threshold we use.

4.2 Physical Interpretation

Taken together, these results support a feedback-regulated picture of LyC escape in high-redshift galaxies. Star formation proceeds in bursty episodes driven by gas accretion and gravitational instabilities. During the early stages of a burst, newly formed massive stars remain embedded in dense gas clouds that absorb ionizing radiation. As feedback processes disrupt these clouds and drive outflows, the ISM becomes increasingly porous, enabling LyC photons to escape along low-density channels. The resulting delay between star formation and LyC escape naturally produces the observed time-lag signature in the simulations.

The strength of this cyclic coupling depends strongly on galaxy mass. In massive halos, the deeper gravitational potential well confines the gas reservoir, allowing repeated cycles of gas accumulation, star formation, and feedback-driven clearing. In lower-mass systems, stellar feedback can more easily expel gas from the galaxy, leading to a more diffuse and irregular ISM structure and weakening the temporal coupling between star formation and escape fraction.

4.3 Implications for Observations and Reionization

These findings have important implications for observational studies of galaxies during the Epoch of Reionization. Because direct detection of LyC radiation is extremely challenging at high redshift, identifying reliable secondary tracers remains a key goal for current and future observational programs. The correlations identified in this work suggest that quantities such as sSFR, O_{32}, and emission-line luminosities may provide indirect constraints on LyC escape.

However, the significant scatter present in many of these relations also highlights the challenges in predicting LyC escape from single observables. The stochastic geometry of the ISM and the time-dependent nature of feedback-driven clearing processes imply that LyC escape is inherently variable, and depends on many physical processes and gas geometry of the ISM. The escape fraction lags behind the burstiness parameter, sSFR, because of the surrounding. Although sSFR is not an observable, the LyC escape fraction still depicts a positive lag with moderate cross-correlation with an observational signature, which corresponds to to sSFR.

However, this work aims to establish physically motivated connections between observable galaxy properties and the escape of ionizing radiation. These results provide a framework

for interpreting upcoming observations of high-redshift galaxies from facilities such as the *James Webb Space Telescope* (*JWST*) and for constraining the role of galaxies in driving cosmic reionization.

4.4 Future Work

Several avenues remain for further investigation. Future work could extend the analysis to larger simulation samples in order to better characterize the dependence of LyC escape on galaxy mass, environment, and redshift. Additionally, incorporating more detailed modelling of dust, gas kinematics, and radiative feedback may help refine predictions for observational tracers. Furthermore, similar analysis can be extended with other metal lines of silicon and nitrogen, looking for secondary tracers using stellar continuum absorption. Statistically, future prospects remain to extend the analysis to the parent THESAN simulations, to get better statistical relations, and get a much robust analysis and relations.

On the observational side, upcoming facilities and surveys will provide increasingly detailed measurements of emission lines and star formation indicators in high-redshift galaxies. Combining such observations with synthetic observables from cosmological simulations will be essential for developing a more comprehensive understanding of the physical processes governing LyC escape. Ultimately, connecting theoretical models with observational diagnostics will be crucial for resolving the long-standing question of how galaxies contributed to the reionization of the Universe.

In summary, this work demonstrates that LyC escape is fundamentally a time-dependent process regulated by feedback-driven restructuring of the ISM. The presence of a measurable delay between star formation and LyC escape, along with its dependence on galaxy mass, provides a new framework for interpreting ionizing radiation leakage in galaxies. These results highlight the importance of temporal analysis in understanding reionization-era galaxies and establish a direct link between theoretical models and observable diagnostics.

Bibliography

[1] B. A. Whitney. Monte carlo radiative transfer. *Bulletin of the Astronomical Society of India*, 39(1):101–127, 3 2011.

[2] R. Kannan, E. Garaldi, A. Smith, R. Pakmor, V. Springel, M. Vogelsberger, and L. Hernquist. Introducing the THESAN project: radiation-magnetohydrodynamic simulations of the epoch of reionization. *Monthly Notices of the Royal Astronomical Society*, 511(3):4005–4030, 2022.

[3] V. Mauerhofer, A. Verhamme, J. Blaizot, T. Garel, T. Kimm, L. Michel-Dansac, and J. Rosdahl. UV absorption lines and their potential for tracing the Lyman continuum escape fraction. *Astronomy & Astrophysics*, 12 2020.

[4] Aaron Smith, Rahul Kannan, Sandro Tacchella, Mark Vogelsberger, Lars Hernquist, Federico Marinacci, Laura V. Sales, Paul Torrey, Hui Li, Yuan-Chen Yeh, and Jia Qi. The physics of Lyman-alpha escape from disc-like galaxies. *Monthly Notices of the Royal Astronomical Society*, 9 2022.

[5] Aaron Smith, Chalence Safranek-Shrader, Volker Bromm, and Miloš Milosavljević. The Lyman-alpha signature of the first galaxies. *Monthly Notices of the Royal Astronomical Society*, 3 2015.

[6] Bruce T. Draine. *Physics of the Interstellar and Intergalactic Medium*. Princeton University Press, 2011.

[7] George B.. Rybicki and Alan P.. Lightman. *Radiative processes in astrophysics*. Wiley-VCH, 2004.

[8] Rahul Kannan, Ewald Puchwein, Aaron Smith, Josh Borrow, Enrico Garaldi, Laura Keating, Mark Vogelsberger, Oliver Zier, William McClymont, Xuejian Shen, Filip Popovic, Sandro Tacchella, Lars Hernquist, and Volker Springel. Introducing the THESAN-ZOOM project: radiation-hydrodynamic simulations of high-redshift galaxies with a multi-phase interstellar medium. *The Open Journal of Astrophysics*, 10 2025.

[9] Cody A Carr, Aaron Smith, Viraj Pandya, Christopher C. Hayward, Mason Huberty, Claudia Scarlata, and Renyue Cen. Evaluating Mass Outflow Rate Estimators in FIRE-2 Simulations: Towards a Self-Consistent Framework for Spectral Line Based Predictions. *\apj*, 3 2025.

[10] William McClymont, Sandro Tacchella, Aaron Smith, Rahul Kannan, Ewald Puchwein, Josh Borrow, Enrico Garaldi, Laura Keating, Mark Vogelsberger, Oliver Zier, Xuejian Shen, Filip Popovic, and Charlotte Simmonds. The THESAN-ZOOM project: Burst, quench, repeat – unveiling the evolution of high-redshift galaxies along the star-forming main sequence. *Monthly Notices of the Royal Astronomical Society*, 2 2026.

[11] The Thesan Collaboration. Thesan-Zooms.

[12] Gergö Popping, Rachel S. Somerville, and Maud Galametz. The dust content of galaxies from z = 0 to z = 9. *Monthly Notices of the Royal Astronomical Society*, 6 2017.

[13] Aaron Smith. COLT docs.